

# Effective programming of a photonic processor with complex interferometric structure

I.V. Kondratyev<sup>1</sup>, K.N. Urusova<sup>1</sup>, A.S. Argenchiev<sup>1</sup>, N.S. Klushnikov<sup>1</sup>, S.S. Kuzmin<sup>1,2</sup>, N.N. Skryabin<sup>1,2</sup>,

A.D. Golikov<sup>3</sup>, V.V. Kovalyuk<sup>3,4</sup>, G.N. Goltsman<sup>2,3</sup>, I.V. Dyakonov<sup>1,2</sup>, S.S. Straupe<sup>1,2</sup>, and S.P. Kulik<sup>1</sup>

<sup>1</sup>*Quantum Technology Centre and Faculty of Physics, M. V. Lomonosov Moscow State University, 1 Leninskie Gory, Moscow, 119991, Russia*

<sup>2</sup>*Russian Quantum Center, 30 Bolshoy Boulevard, building 1, Moscow, 121205, Russia*

<sup>3</sup>*Department of Physics, Moscow State Pedagogical University, Moscow 119992, Russia and*

<sup>4</sup>*Laboratory of Photonic Gas Sensors, University of Science and Technology MISIS, Moscow 119049, Russia*

(\*iv.kondratjev@physics.msu.ru)

(Dated: August 22, 2025)

Reconfigurable photonics have rapidly become an invaluable tool for information processing. Light-based computing accelerators are promising for boosting neural network learning and inference [1–3] and optical interconnects are foreseen as a solution to the information transfer bottleneck in high-performance computing [4–6]. In this study, we demonstrate the successful programming of a transformation implemented using a reconfigurable photonic circuit with a non-conventional architecture. The core of most photonic processors is an MZI-based architecture [7, 8] that establishes an analytical connection between the controllable parameters and circuit transformation. However, several architectures [9, 10] that are substantially more difficult to program have improved robustness to fabrication defects. We use two algorithms that rely on different initial datasets to reconstruct the circuit model of a complex interferometer, and then program the required unitary transformation. Both methods performed accurate circuit programming with an average fidelity above 98%. Our results provide a strong foundation for the introduction of non-conventional interferometric architectures for photonic information processing.

## I. INTRODUCTION

Integrated photonics have already significantly impacted in various areas of science and technology, including communication [11–13], quantum and classical computing [14], optical neural networks [2, 3, 15], and life sciences [16, 17]. The key feature of integrated photonic systems that drives the growth of interest is the ability to route and manipulate light states using on-chip phase modulation. Information processing tasks use interferometric waveguide circuits that enable programmable encoding of information processing algorithms using light. The benefits are the larger operational bandwidth of photonic devices and a better energy efficiency per operation [18–20].

In this study, we target photonic device programming for information processing. A typical photonic chip for this purpose includes multiple power splitters and phase shifters comprising a large multiarm interferometer [21–23]. Once a photonic processor has been fabricated, it must be properly calibrated to implement a unitary transformation on demand. This process is challenging if the interferometric circuit architecture includes complex elements, such as multiport power-splitting circuits [2, 3, 24].

The transformation of the interferometer is described by a unitary transfer matrix  $U$ , which depends on the phases between different paths  $U = U(\vec{\varphi})$ . Typically, the procedure for calibrating phase shifters involves injecting coherent light and control signal through the phase shifters one by one and recording the output interference pattern. The data collected are fitted with an interferometer model accompanied by phase functions  $\varphi(X)$ , where  $X$  is a control signal (typically current  $I$  or voltage  $V$ ). The result of the procedure are the exact functions  $\varphi(X)$  that characterize each phase shifter.

Common photonic architectures rely on a Mach-Zehnder interferometer (MZI) as a building block [7, 8, 25, 26]. This

class of architectures bases on the well-known isomorphism of the MZI transfer matrix and the arbitrary unitary  $SU(2)$  rotation. Within MZI-based architectures, the calibration can be performed for each interferometer one after another, as it is possible to isolate the effect of each individual block [15, 19, 21, 27–29].

However, this strategy is not applicable to interferometers with other types of building blocks. For example, using multiport beamsplitters [10] or beamsplitter meshes [30] turns out to be beneficial in minimizing the effects of fabrication imperfections. Interferometers of this kind have already been demonstrated [9, 31, 32] but programming a desired unitary transformation remains an unresolved challenge. The well-known issue of the crosstalk between multiple tunable phase shifters complicates the unitary programming problem even more by rendering easy calibration procedures inaccurate even in simple architectures such as [7, 8].

The task of programming a unitary transfer matrix of a reconfigurable photonic system can be approached differently. The first step would be to infer the parameters of the photonic system and construct its digital replica. The parameters include both characteristics of optical components, such as, for example, the power splitting ratio of the beamsplitters, and the coefficients connecting tunable phase shifts with applied control signal. Several recent studies followed these guidelines [23, 29, 33–35] and demonstrated programming transfer matrices of MZI mesh-based interferometric systems.

However, there exists substantial practical interest in interferometers with  $n \times n$  waveguide splitters [36–38], as they can be used as a powerful tool for photonic convolutional networks and random matrix generation [2, 39]. We will call the interferometers consisting of such couplers multiport interferometers. There is no straightforward approach to enable programming unitary transfer matrices of the interferometer with  $n \times n$  splitters.

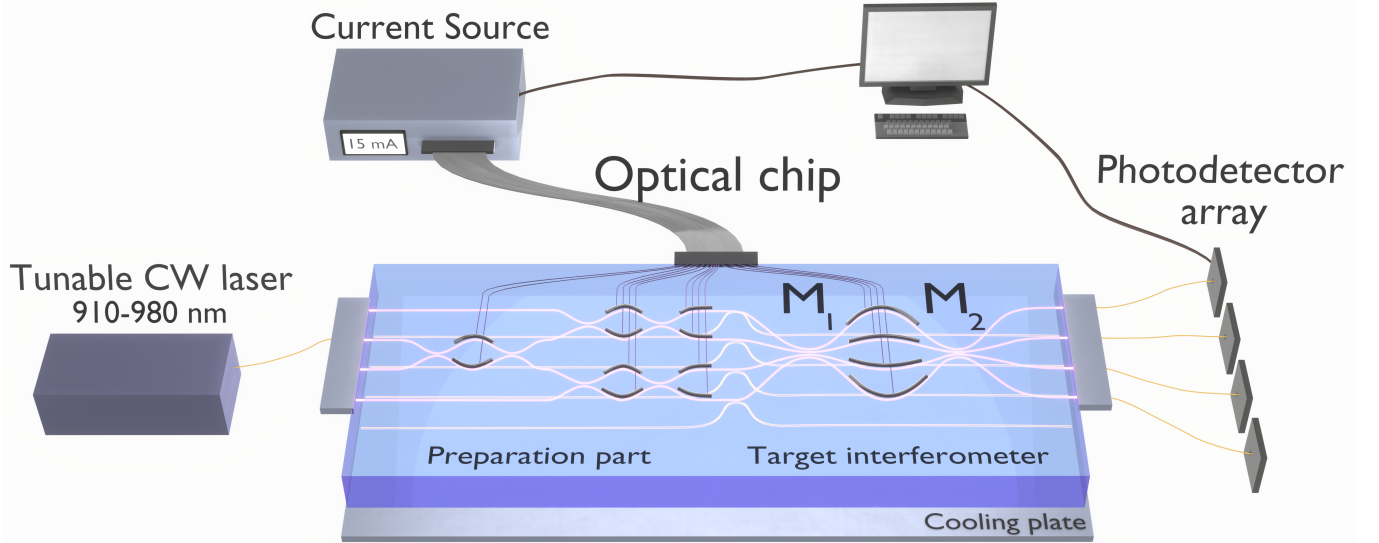


FIG. 1. Schematic photonic chip structure. The preparation part, consisting of three cascaded MZIs and a target complex interferometer consisting of two  $4 \times 4$  multiport couplers sandwiching three tunable phase shifters, are both in the same fused silica sample. Laser light is injected into the second input port of the chip. This allows for the preparation of an arbitrary optical distribution of light among the four input ports of the target interferometer. The MZIs in the interferometer can be individually calibrated using auxiliary waveguides that are weakly coupled to the output section of the preparation part of the interferometer. Auxiliary waveguides lie  $35 \mu\text{m}$  below the main waveguide plane with preparation and target interferometers. Each auxiliary waveguide is only coupled to the corresponding waveguide of the preparation interferometer and only at its output region.

It is worth mentioning that many of the existing studies on MZI-based interferometer programming have not used the actual matrix fidelity measure to demonstrate the ability to achieve the desired unitary matrix set on a chip. Instead, in these studies, another metric called amplitude fidelity was used [19, 23, 28, 34, 35], which is inherently insensitive to the angles of the unitary transformation that are crucial for the evolution of multiphoton states through linear optical interferometers. However, amplitude fidelity has been argued to contain nearly the same amount of information, demonstrating the universal capabilities of the interferometers under study [29].

Several recent theoretical proposals demonstrated how to program an arbitrary complex interferometer in two steps [40, 41]. In the first step, the digital model of the interferometer is inferred from the experimental data set, and the digital model afterwards serves as a reliable tool to determine the phase configuration corresponding to the required unitary transfer matrix. Both methods require precise control of the phase shifts  $P(\vec{\phi})$  that in turn demand fine calibration  $\vec{\phi} = \vec{\phi}(\vec{X})$  of the phase modulators.

Herein, we present the programming algorithm based on the reconstructed digital model of the photonic interferometer with arbitrary architecture. We used the algorithm to demonstrate the reconfigurable operation of the 4-mode multiport photonic processor. To verify the algorithm, we experimentally set and measured 100 random *unitary* transformations on the chip and compared them with those predicted using the chips' digital model. We used the true matrix fidelity measure for comparison and reported average fidelity  $99.6 \pm 0.2$ .

## II. METHODS

### A. Optical Chip Design

Our photonic chip was manufactured using femtosecond laser writing (FSLW) in a fused silica glass sample [42]. The description of the waveguide fabrication regime can be found in Appendix A. The single-mode waveguide structure of the chip contained a target  $4 \times 4$  multiport interferometer and a preparation interferometer. The preparation interferometer is a mesh of three MZIs which can set an arbitrary amplitude distribution at the output of the preparation part. We use the preparation interferometer as a tool for calibrating the target interferometer and probing its transfer matrix. Both the preparation and the target interferometers are equipped with tunable thermo-optical phase shifters, which are also fabricated using the femtosecond laser writing setup.

The FSLW technology allows us to create waveguides inside a three-dimensional space. This feature enables us to write four auxiliary waveguides  $35 \mu\text{m}$  below the main waveguide plane. These waveguides are evanescently coupled to the output section of each waveguide of the preparation interferometer. We used these waveguides to monitor the amplitudes fed to the input of the target interferometer, which is a crucial requirement for reconstruction of the digital model of the target interferometer.

The light from the chips' output ports was collected using a fiber array, and the corresponding optical power was then measured using four photodetectors. The input fiber and the

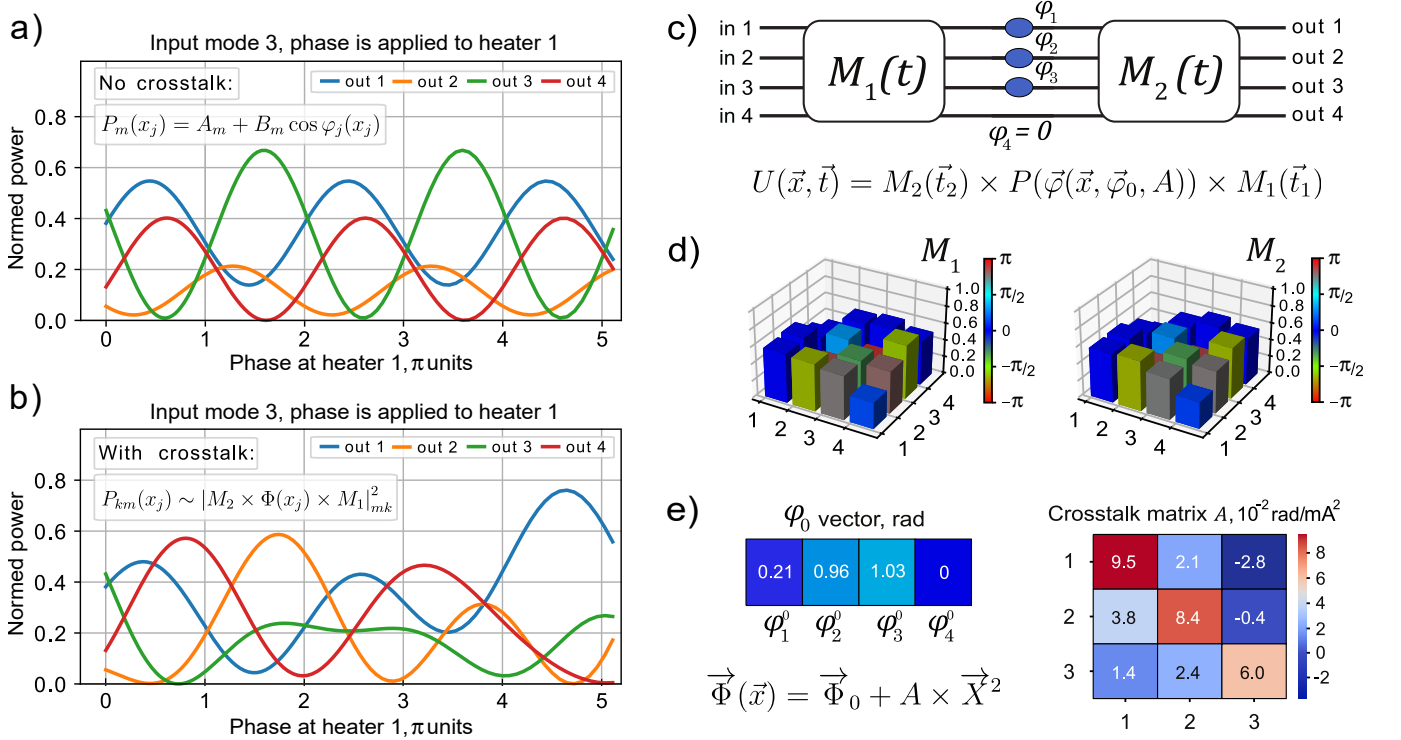


FIG. 2. a) Typical output optical power dependence  $P_m(\varphi(x_j))$  in cases a) without crosstalk and b) with mutual crosstalk between adjacent phase-shifters. This illustration shows the numerical modeling of the calibration of the phase shifter  $\varphi_1$  when coherent radiation is injected into the third input port of the target interferometer (see Fig. 1). In the absence of crosstalk, all  $P_m(\varphi(x_j))$  curves are sinusoidal with an equal period. However, in the presence of crosstalk, each  $P_m(\varphi(x_j))$  becomes a complex and non-periodic curve. c) A schematic illustration of the digital model of the target interferometer and its parametrization. The chips' unitary transformation  $U$  was decomposed in three blocks: two mode-mixing blocks  $M_{1,2}$  and a phase shift layer  $P(\vec{\varphi}(\vec{x}, \vec{\varphi}_0, A))$  between them. Both mode-mixing blocks  $M_{1,2}$  were parameterized by a triangular mesh of MZIs [7], which required 9 real parameters  $t_j$  in the range  $t_j \in [0, 2\pi]$ . d) Mode-mixing unitary matrices  $M_{1,2}$  obtained from the simultaneous approximation of all calibration data. e) The  $\Phi_0$  vector of the bias phase shifts and the matrix of crosstalk  $A$  obtained from the simultaneous approximation of the calibration data.

output fiber array were mounted on high-precision six-axis positioners. We could use the output positioner to switch between the output of the target interferometer and the auxiliary waveguides. The structure of the chip and the experimental setup are shown schematically in Fig. 1.

Calibration of the MZI-based interferometer is a known procedure that is performed by individually calibrating each of its constituent MZIs [19, 21, 27, 28]. We used the same principles to calibrate the preparation interferometer. More details on the optical chip design and preparation interferometer calibration can be found in Appendices B and C.

The target interferometer consists of two  $4 \times 4$  multiport couplers sandwiching three tunable phase shifters. The optical interferometers with this kind of architecture were studied in [10]. The unitary transformation of the target interferometer can be expressed as

$$U(\vec{\varphi}) = M_2 \times P(\vec{\varphi}) \times M_1, \quad (1)$$

where  $M_{1,2}$  are the unitary matrices corresponding to each of the  $4 \times 4$  multiport couplers, which we also refer to as constant mode mixing blocks,  $\vec{\varphi} = \{\varphi_1, \varphi_2, \varphi_3\}$  is a vector of three phase shifts and  $P(\vec{\varphi}) = \text{diag}(e^{i\varphi_1}, e^{i\varphi_2}, e^{i\varphi_3}, 1)$  is a diagonal matrix of the phaseshifting layer. The key task for suc-

cessful implementation of the programming procedure is the reconstruction of the two matrices  $M_{1,2}$  and  $P(\vec{\varphi}(\vec{X}))$ , where  $\vec{X} = \{x_1, x_2, x_3\}$  are the electrical currents applied to thermo-optical phase shifters.

## B. Target interferometer calibration

The calibration of tunable phase shifters in an  $N$ -port reconfigurable interferometer starts with injecting coherent laser light into the sample. For each input port, the electrical current  $x_j$  through the  $j$ -th phase shifter is swept within a range of values while measuring the optical power  $P_m$  from each output port  $m$  of the interferometer  $P_m = P_m(x_j)$ .

The ideal scenario occurs when  $j$ -th modulator affects only the corresponding shift on the interferometer  $\varphi_j = \varphi(x_j)$ . In this case, the output power  $P_m$  obeys the periodic law

$$P_m(x_j) = A_m + B_m \cos \varphi_j(x_j), \quad (2)$$

where  $A_m$  and  $B_m$  are real constants (independent of  $x_j$ ) depending on the inner interferometer structure, in our case the matrices  $M_{1,2}$  describing the multiport splitters. The  $\varphi =$

$\varphi_j(x_j)$  is a specific dependence of the  $j$ -th phase shift on the corresponding driving signal  $x_j$  and is generally assumed to be a polynomial function of  $x_j$ . For example, in the case of a thermo-optical phase shifter,  $\varphi_j(x_j) = \varphi_j^0 + \alpha_j x_j^2$  because the induced phase shift is directly proportional to the thermal power dissipated by a resistive electrode. A typical  $P_m(\varphi(x_j))$  behavior in the absence of crosstalk is shown in Fig. 2a.

After measuring  $P_m(x_j)$ , the approximation of the experimental data with (2) provides the calibration parameters  $\varphi_j^0$  and  $\alpha_j$  for a specific tunable phase-shifter. Note that the specific values of the constants  $A_m$  and  $B_m$  are not important in this procedure, and the most critical parameters for each phase-shifter are the corresponding  $\varphi_j^0$  and  $\alpha_j$ . After obtaining all calibration parameters  $\varphi_j^0$  and  $\alpha_j$  for each  $j$ -th tunable phase shifter, the algorithms [40, 41] can be implemented to reconstruct  $M_{1,2}$ . Once the  $M_{1,2}$  are inferred, then a full digital model of the photonic chip is available to find a phase configuration corresponding to a required unitary transfer matrix.

However, in most real optical chips, even those fabricated using the most advanced technology [28], there is often an effect of mutual cross-influence between different phase shifters. This can occur because of thermal or electrical crosstalk. Due to the crosstalk effect, the optical power  $P_m$  from the  $m$ -th output port of the chip can no longer be described by 2 because the approximation constants  $A_m$  and  $B_m$  are functions of  $x_j$ , as well as of the indices of the input and output ports of the interferometer. This leads to a complex and non-periodic dependence  $P_m(x_j)$ . Figure 2b shows the typical dependency  $P_m(x_j)$  in the presence of crosstalk.

In our optical chip, we used thermo-optical phase shifters for which a significant crosstalk effect between adjacent heaters was observed. Due to the presence of mutual coupling between different phase shifters, the phase shift  $\varphi_i$  induced in the  $i$ -th heater depends not only on the corresponding current  $x_i$  but also on all currents  $x_j$  applied to other heaters (which may influence the  $i$ -th phase shift):

$$\varphi_i(\vec{x}) = \varphi_0^{(i)} + \sum_j \alpha_{ij} x_j^2, \quad (3)$$

where  $x_j$  is the current applied to  $j$ -th heater,  $\varphi_0^{(i)}$  is a constant bias phase shift that exists in the particular interferometer arm, and  $\alpha_{ij}$  is a constant that determines the strength of the effect of the  $j$ -th heater on the  $i$ -th phase shifter. The relation between the phases and the currents flowing through the heaters can be rewritten in matrix form as follows:

$$\vec{\Phi}(\vec{x}) = \vec{\Phi}_0 + A \times \vec{X}^2, \quad (4)$$

where  $\vec{\Phi} = \{\varphi_1, \varphi_2, \varphi_3\}^T$  is a column vector of the phase shifts to be set,  $\vec{\Phi}_0 = \{\varphi_1^0, \varphi_2^0, \varphi_3^0\}^T$  is the column vector of the bias phase shifts,  $A = \{\alpha_{ij}\}$  is a crosstalk matrix containing all nine crosstalk constants  $\alpha_{ij}$ ,  $i, j = 1, 2, 3$ , and  $\vec{X}^2 = \{x_1^2, x_2^2, x_3^2\}^T$  is a column vector of squared current values.

Therefore, according to (3), if only one  $x_j$  is varied, it will affect all three phase shifts  $\varphi_i$  simultaneously, leading to a complex and nonperiodic dependence of the output optical power on the applied current  $x_j$  (see Fig. 2b). Nevertheless,

if coherent light is injected into the  $k$ -th input port of the photonic chip, the output optical power at the  $m$ -th output port can be described in terms of the  $m, k$ -th element of the unitary matrix of the interferometer:

$$P_{km}(x_j) \sim |M_2 \times \vec{\Phi}(x_j) \times M_1|_{mk}^2, \quad (5)$$

which can be used to fit the corresponding experimental data, with both  $M_1$ ,  $M_2$ , and  $\vec{\Phi}_0$ , and the matrix of crosstalk constants  $A$  as optimization parameters.

Moreover, any experimentally measured optical power  $P_{km}$  from the applied current for any input  $k$  and output  $m$  ports of the interferometer and for any heater  $j$  must obey (5) with the same interferometer parameters  $M_{1,2}$ ,  $\vec{\Phi}_0$  and  $A$ , as they are all generated by the same photonic chip, described by its unitary matrix  $U$ . Once all possible optical powers from the applied current dependencies,  $P_{km}(x_j)$ , have been experimentally measured for each  $k, m$ , and  $j$ , they all can be simultaneously approximated using a single interferometer model, determining the optical chips' constituents  $M_{1,2}$  and the necessary calibration relations between all currents and phase shifts  $\vec{\Phi}_0$  and  $A$ . The key points of the approximation over the whole dataset are given in the next subsection.

### C. The target interferometer model

The approximation of the whole data set  $P_{km}(x_j)$  in the form of (5) requires appropriate parameterization of the optical chip transfer matrix  $U(\vec{x})$  as a function of the applied currents:

$$U(\vec{x}, \vec{t}) = M_2(\vec{t}_2) \times P(\vec{\Phi}(\vec{x}, \vec{\Phi}_0, A)) \times M_1(\vec{t}_1), \quad (6)$$

where  $\vec{t}_{1,2} = \{t_1, \dots, t_N\}$  are two sets of real parameters that determine  $M_{1,2}$ ,  $P(\vec{\Phi}(\vec{x}, \vec{\Phi}_0, A)) = \text{diag}(e^{i\varphi_1}, e^{i\varphi_2}, e^{i\varphi_3}, 1)$  is a diagonal matrix of the phase shifts (see Fig. 2c). In turn, the phase shifts depend on the currents  $x_j$  and the calibration parameters  $\varphi_j^{(0)}$  and  $\alpha_{ij}$ :

$$\begin{pmatrix} \varphi_1 \\ \varphi_2 \\ \varphi_3 \end{pmatrix} = \begin{pmatrix} \varphi_1^{(0)} \\ \varphi_2^{(0)} \\ \varphi_3^{(0)} \end{pmatrix} + \begin{pmatrix} \alpha_{11}, \alpha_{12}, \alpha_{13} \\ \alpha_{21}, \alpha_{22}, \alpha_{23} \\ \alpha_{31}, \alpha_{32}, \alpha_{33} \end{pmatrix} \times \begin{pmatrix} x_1^2 \\ x_2^2 \\ x_3^2 \end{pmatrix}, \quad (7)$$

where later two are to be experimentally determined.

For mode-mixing blocks  $M_{1,2}$  we used the well-known unitary parameterization [7] that for the  $4 \times 4$  port interferometer requires nine real parameters varying from 0 to  $2\pi$  each (see Appendix D for details). The total number of real parameters for our photonic chip then equals to 30, including  $9 \times 2 = 18$  parameters for  $M_{1,2}$ , 3 bias phases  $\varphi_j^{(0)}$ , and 9 crosstalk constants  $\alpha_{ij}$ .

An adequate initial guess for the optimization parameters is important because the global optimization process experiences difficulties converging to the global minimum using a random initial seed. The specific physical properties of the experimental system should be considered when setting the limits of the parameter values.



### III. EXPERIMENTAL RESULTS

We gathered the data set  $P_{km}(x_j)$  and ran the approximation which yielded  $M_1$  and  $M_2$ ,  $\vec{\Phi}_0$ , and  $A$ , which are illustrated in Fig. 2d,e. Although no additional constraints were set for the parameterization of  $M_1$  and  $M_2$  they appeared to be almost equal  $M_1 \approx M_2$  as shown in Fig. 2d, which reflects the fact that physically in our optical chip both  $M_{1,2}$  were realized as  $4 \times 4$  directional couplers with identical geometrical parameters (i.e. waveguide shapes, distances between waveguides and laser exposure parameters). Moreover, from Fig. 2e we can see that the bias phases satisfy  $\varphi_1^0 \approx \varphi_4^0$  and  $\varphi_2^0 \approx \varphi_3^0$ , which can also be explained by the actual geometry of the phase shift layer  $P(\varphi)$  on our chip (see Fig. 1).

In the phase shift layer of the target interferometer, the first and fourth waveguides have the same length, while the second and third waveguides also have the same length but are shorter than the first and fourth. This results in non-zero bias phase shifts, as shown in Fig. 2e.

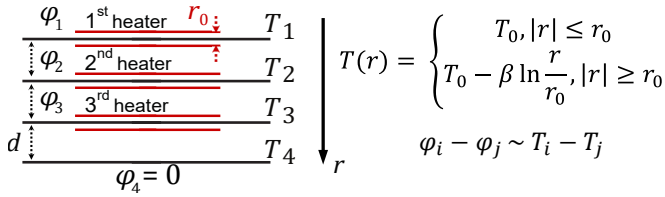


FIG. 3. Guidelines for the estimation of relations between the crosstalk elements  $A = \{\alpha_{ij}\}$ .

The reconstructed elements of the crosstalk matrix  $A$  (see Fig. 2e) correlate with our assumption about their mutual relation based on the geometry of the optical structure. The negative values of some of the elements are also predicted by our simple model. The qualitative estimation of the relative magnitudes of  $\alpha_{ij}$  can be made using the linearity of the heat equation, the assumption of logarithmic temperature decay with distance from the heater and the proportionality between the phase and temperature differences  $\varphi_i - \varphi_j \sim T_i - T_j$ . Assuming (endless) parallel straight heaters with a width of  $r_0$  right above (endless) parallel straight waveguides are equally separated by  $d$  from each other (see Fig. 3), one can derive the following form of the crosstalk matrix  $A$ :

$$A = \{\alpha_{ij}\} = \alpha_0 \begin{pmatrix} \ln \frac{3d}{r_0} & \ln 2 & -\ln 2 \\ \ln 3 & \ln \frac{2d}{r_0} & 0 \\ \ln \frac{3}{2} & \ln 2 & \ln \frac{d}{r_0} \end{pmatrix}, \quad (8)$$

where  $\alpha_0$  is a constant (see Appendix D for more details).

#### A. Testing the digital model of the chip

To verify the validity of our digital interferometer model, we perform the following procedure. We sampled a set of 100 random current configurations  $\{x_1^{(n)}, x_2^{(n)}, x_3^{(n)}\}$  ( $n = \overline{1, 100}$ ) in

the range of 0 to 15 mA and applied them to our photonic chip. For each set of currents, the chips' unitary transformation  $U_{exp}^{(n)}$  was measured directly using coherent CW radiation [43, 44] (see Appendix E for details). On the other hand,  $U^{(n)}$  can be simulated from the digital chip model (6) and compared to the measured one by the matrix fidelity measure:

$$F(U_{exp}, U_{sim}) = \frac{\text{Tr}(U_{exp} \times U_{sim}) \text{Tr}(U_{sim} \times U_{exp})}{\text{Tr}(U_{exp} \times U_{exp}) \text{Tr}(U_{sim} \times U_{sim})}, \quad (9)$$

The results are shown in Fig. 4a. The average fidelity of 100 measured unitary matrices is  $99.6 \pm 0.2\%$ . Figure 4b shows the measured unitary matrices and the chip model unitary matrices for specific currents on a chip, with the lowest mutual matrix fidelity among all sets. Remarkably, the lowest fidelity between the measured and simulated unitaries was 99.2%. This result clearly demonstrates the high quality of the digital model of our photonic chip.

#### B. Optical port-to-port permutations in a wide range

The procedure described above for the experimental calibration of the photonic chip (and programming the chip at the same time) requires simply injecting coherent radiation into each mode of the chip, applying current to a specific heater, and recording the optical power from all output ports. After the successful approximation of the entire data set of the calibration data collected, a complete digital model of the chip is obtained. In this procedure, the wavelength  $\lambda$  determines the resulting unitary transformation  $U = U(\lambda)$  due to the spectral features of the mode-mixing blocks and the spectral dependence of the phase shifts. The reconstruction of the digital model can be repeated with different wavelengths  $\lambda_{new}$  to retrieve the chip model  $U = U(\lambda_{new})$ . The multiport interferometer architecture [10] was theoretically proven to be robust to the deviations of the mode-mixing block transfer matrices. By implementing the same operation, the optical port-to-port switching, using interferometers with different mode-mixing blocks we highlight the robustness feature of the multiport architecture.

To demonstrate the wide spectral range of our photonic chip capabilities and its potential to perform predefined optical transformations with practical applications, we have experimentally performed optical switching at seven different wavelengths between 915 and 975 nanometers. The optical switching is a particularly demanding task for an interferometric circuit, especially based on MZI blocks, because it requires precise calibration of the power couplers and phase shifters. We first calibrated our optical chip for seven wavelengths using a continuously tunable CW laser (Toptica CTL 950), which has a range of wavelengths between  $\lambda_m = 915$  and 975. We then obtained digital models  $U(\vec{x}, \lambda_m)$  for each of these wavelengths. Then, using the known digital model of the chip,  $U(\vec{x}, \lambda_m)$ , we use optimization (the Python `scipy.optimize.minimize` function) to find a current configuration,  $\{x_1, x_2, x_3\}$ , which realizes a particular optical switch for each wavelength and each input port. Numerical optimization

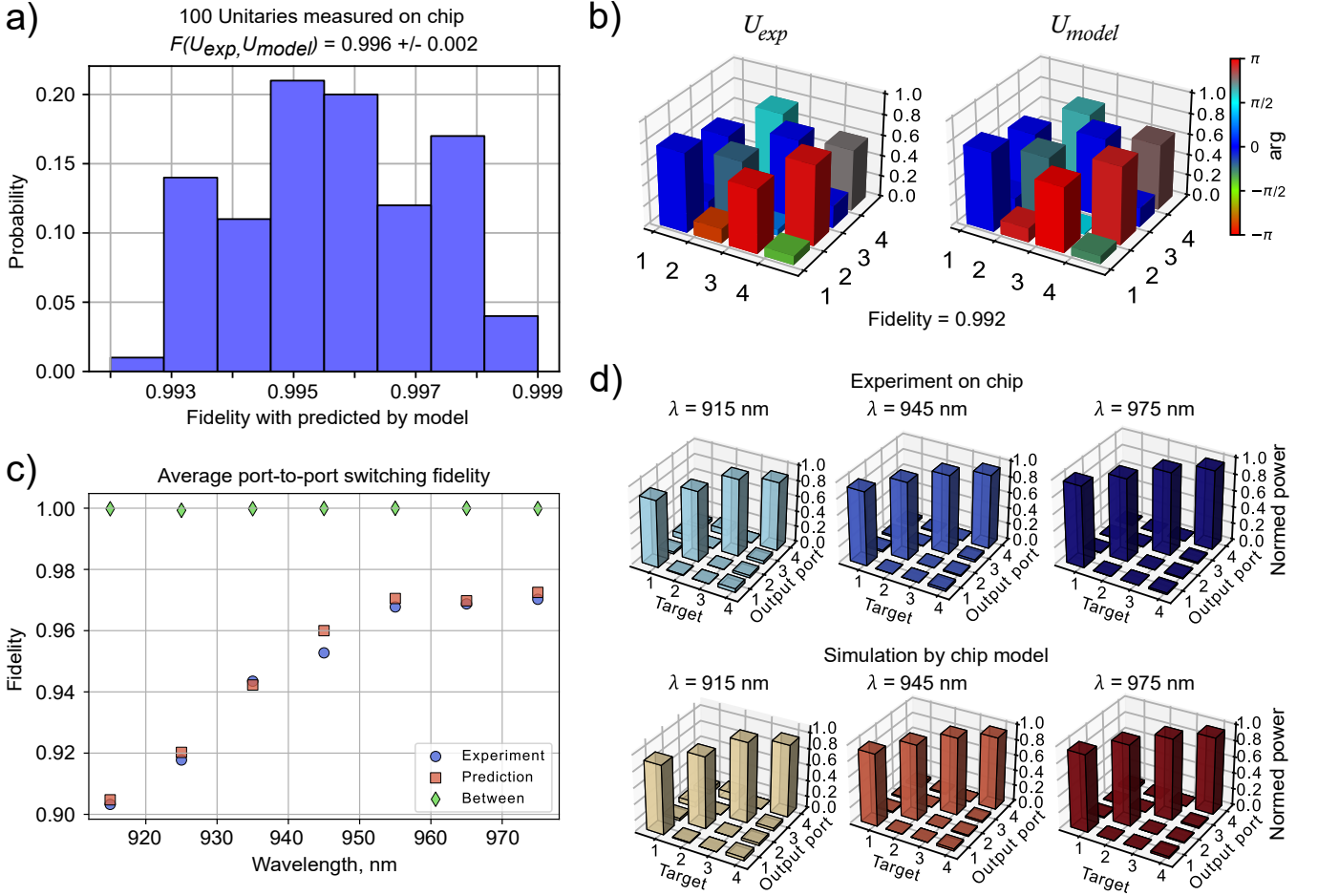


FIG. 4. The results of the digital model of the optical chip quality testing. a) The Matrix fidelity between 100 measured *unitaries* on chip and the corresponding unitaries simulated using the chip’s model. b) An example of a pair of measured-simulated unitaries with the lowest value of matrix fidelity 99.2%. All the other 99 pairs of measured-simulated unitaries have greater matrix-fidelity values. c) Graph of average optical port-to-port switching fidelities for different wavelengths of coherent radiation. d) Histograms of the power distribution at the output ports of the optical chip, reconfigured for one-to-one switching to a specific output, are shown for the first input port and three wavelengths.

was used to minimize the infidelity function  $Inf = 1 - F$  with fidelity defined as

$$F(\vec{x}, \vec{y}) = \left( \sum_j \sqrt{x_j y_j} \right), \quad (10)$$

where  $\vec{x}$  and  $\vec{y}$  are two column vectors, with a unit sum representing the normalized measured and target output power distributions at the output of the optical chip, respectively.

Finally, the optimized current configurations were set on the photonic chip, and the corresponding optical switching was observed. Figure 4c shows the average port-to-port switching fidelity among all switching configurations for each wavelength of coherent radiation. It can be seen that while the absolute values of the average port-to-port switching fidelities are not ideal (all less than 0.98) for each wavelength, the mutual average fidelity between the measured output power distribution and its prediction by a digital model is at least 0.99 (see Appendix F for details). This clearly shows that if the target interferometer is unable to implement a required transfer

matrix, the digital model provides an accurate estimation of the expected fidelity.

It is worth noting that although the necessary currents for the realization of a particular unitary transformation  $U(\vec{x})$  on the chip were obtained through optimization, this optimization process was not performed directly on the chip, as previously reported in [32]. Instead, it was conducted by using a digital chip model. Therefore, using a digital model effectively saves the resources of the target photonic chip and helps extend its active lifetime by avoiding the need for excessive reconfiguration. Additionally, in Appendix G we discuss the scalability of the proposed calibration method which in terms of the required single heater calibrations grows quadratically with the number of ports  $N$  in the chip, and in Appendix H we describe an alternative optical chip calibration procedure based on the training of an architecture-agnostic model on 100 measured unitary matrices on the chip.

Finally, we successfully demonstrate the implementation of 100 random unitary matrices on a chip and the broadband optical port-to-port switching. These results validate our digital

model and demonstrate that the optical chip with its complex interferometric structure was successfully programmed. In the future, we plan to demonstrate the implementation of Haar random unitaries on our chip and show the potential applicability of our chip in solving information processing tasks.

## ACKNOWLEDGMENTS

The authors acknowledge support from Russian Science Foundation grant 22-12-00353P (<https://rscf.ru/en/project/22-12-00353P/>); V.K., A.D. and G.G. acknowledge support of the Ministry of Science and Higher Education of the Russian Federation FSME-2025-0004 (PICs fabrication).

- 
- [1] X. Xiao, M. B. On, T. Van Vaerenbergh, D. Liang, R. G. Beausoleil, and S. Yoo, *Apl Photonics* **6** (2021).
  - [2] X. Meng, G. Zhang, N. Shi, G. Li, J. Azaña, J. Capmany, J. Yao, Y. Shen, W. Li, N. Zhu, *et al.*, *Nature Communications* **14**, 3000 (2023).
  - [3] J. Cheng, C. Huang, J. Zhang, B. Wu, W. Zhang, X. Liu, J. Zhang, Y. Tang, H. Zhou, Q. Zhang, *et al.*, *Nature Communications* **15**, 6189 (2024).
  - [4] Y. Li, A. Louri, and A. Karanth, in *2021 58th ACM/IEEE Design Automation Conference (DAC)* (IEEE, 2021) pp. 931–936.
  - [5] A. Rizzo, S. Daudlin, A. Novick, A. James, V. Gopal, V. Murthy, Q. Cheng, B. Y. Kim, X. Ji, Y. Okawachi, *et al.*, *IEEE Journal of Selected Topics in Quantum Electronics* **29**, 1 (2022).
  - [6] A. Netherton, M. Dumont, Z. Nelson, J. Koo, J. Jhonsa, A. Mo, D. McCarthy, S. Deckoff-Jones, Y. Gao, N. Pestana, *et al.*, *Photonics Research* **12**, A69 (2024).
  - [7] M. Reck, A. Zeilinger, H. J. Bernstein, and P. Bertani, *Phys. Rev. Lett.* **73**, 58 (1994).
  - [8] W. R. Clements, P. C. Humphreys, B. J. Metcalf, W. S. Kolthammer, and I. A. Walmsley, *Optica* **3**, 1460 (2016).
  - [9] R. Tang, T. Tanemura, and Y. Nakano, *IEEE Photonics Technology Letters* **29**, 971 (2017).
  - [10] M. Y. Saygin, I. V. Kondratyev, I. V. Dyakonov, S. A. Mironov, S. S. Straupe, and S. P. Kulik, *Phys. Rev. Lett.* **124**, 010501 (2020).
  - [11] K. Tanizawa, K. Suzuki, M. Toyama, M. Ohtsuka, N. Yokoyama, K. Matsumaro, M. Seki, K. Koshino, T. Sugaya, S. Suda, G. Cong, T. Kimura, K. Ikeda, S. Namiki, and H. Kawashima, *Opt. Express* **23**, 17599 (2015).
  - [12] L. Lu, S. Zhao, L. Zhou, D. Li, Z. Li, M. Wang, X. Li, and J. Chen, *Opt. Express* **24**, 9295 (2016).
  - [13] K. Suzuki, K. Tanizawa, S. Suda, H. Matsuura, T. Inoue, K. Ikeda, S. Namiki, and H. Kawashima, *Opt. Express* **25**, 7538 (2017).
  - [14] J. Capmany and D. Pérez, *Programmable integrated photonics* (Oxford University Press, 2020).
  - [15] H. Zhang, M. Gu, X. Jiang, J. Thompson, H. Cai, S. Paesani, R. Santagati, A. Laing, Y. Zhang, M.-H. Yung, *et al.*, *Nature communications* **12**, 457 (2021).
  - [16] A. Goel, C. Tung, Y.-H. Lu, and G. K. Thiruvathukal, in *2020 IEEE 6th World Forum on Internet of Things (WF-IoT)* (2020) pp. 1–6.
  - [17] A. Ciceri, G. Corrielli, R. Osellame, F. Bragheri, and P. Paiè, in *Optical Fibers and Sensors for Medical Diagnostics, Treatment, and Environmental Applications XXV* (SPIE, 2025) p. PC133100L.
  - [18] S. Shekhar, W. Bogaerts, L. Chrostowski, J. E. Bowers, M. Hochberg, R. Soref, and B. J. Shastri, *Nature Communications* **15**, 751 (2024).
  - [19] S. Lin, Y. Zhang, Z. Wu, S. Zeng, Q. Gao, J. Li, X. Yu, and S. Yu, *Photonics Research* **12**, A11 (2024).
  - [20] M. A. Butt, B. Janaszek, and R. Piramidowicz, *Sensors International*, 100326 (2025).
  - [21] J. Carolan, C. Harrold, C. Sparrow, E. Martín-López, N. J. Russell, J. W. Silverstone, P. J. Shadbolt, N. Matsuda, M. Oguma, M. Itoh, G. D. Marshall, M. G. Thompson, J. C. F. Matthews, T. Hashimoto, J. L. O'Brien, and A. Laing, *arXiv e-prints*, [arXiv:1505.01182](https://arxiv.org/abs/1505.01182) (2015), [arXiv:1505.01182 \[quant-ph\]](https://arxiv.org/abs/1505.01182).
  - [22] C. Taballione, R. van der Meer, H. J. Snijders, P. Hooijschuur, J. P. Epping, M. de Goede, B. Kassenberg, P. Venderbosch, C. Toebes, H. van den Vlekkert, P. W. H. Pinkse, and J. J. Renema, *arXiv e-prints*, [arXiv:2012.05673](https://arxiv.org/abs/2012.05673) (2020), [arXiv:2012.05673 \[quant-ph\]](https://arxiv.org/abs/2012.05673).
  - [23] A. Barzaghi, M. Bénéfice, F. Ceccarelli, G. Corrielli, V. Galli, M. Gardina, V. Grimaldi, J. Kaczorowski, F. Malaspina, R. Osellame, *et al.*, *arXiv preprint arXiv:2505.01609* (2025).
  - [24] I. Kondratyev, I. Dyakonov, M. Y. Saygin, S. Straupe, and S. Kulik, in *Aip conference proceedings*, Vol. 2241 (AIP Publishing, 2020).
  - [25] K. H. R. Mojaver, B. Zhao, E. Leung, S. M. R. Safaee, and O. Liboiron-Ladouceur, *Optics express* **31**, 23851 (2023).
  - [26] T. G. de Brugière, R. Mezher, S. Currie, and S. Mansfield, *arXiv preprint arXiv:2504.06059* (2025).
  - [27] N. Skryabin, I. Kondratyev, I. Dyakonov, O. Borzenkova, S. Kulik, and S. Straupe, *Applied Physics Letters* **122**, 121102 (2023).
  - [28] C. Taballione, M. C. Anguita, M. de Goede, P. Venderbosch, B. Kassenberg, H. Snijders, N. Kannan, W. L. Vleeshouwers, D. Smith, J. P. Epping, *et al.*, *Quantum* **7**, 1071 (2023).
  - [29] C. Pentangelo, N. Di Giano, S. Piacentini, R. Arpe, F. Ceccarelli, A. Crespi, and R. Osellame, *Nanophotonics* (2024).
  - [30] S. A. Fldzhyan, M. Y. Saygin, and S. P. Kulik, *Opt. Lett.* **45**, 2632 (2020).
  - [31] J. Zhou, J. Wu, and Q. Hu, *Optics Express* **26**, 3020 (2018).
  - [32] I. Kondratyev, V. Ivanova, S. Fldzhyan, A. Argenchiev, N. Kostyuchenko, S. Zhuravitskii, N. Skryabin, I. Dyakonov, M. Saygin, S. Straupe, *et al.*, *Photonics Research* **12**, A28 (2024).
  - [33] S. Bandyopadhyay, A. Sludds, S. Krastanov, R. Hamerly, N. Harris, D. Bunandar, M. Streshinsky, M. Hochberg, and D. Englund, *arXiv preprint arXiv:2208.01623* (2022).
  - [34] A. Fyrrillas, O. Faure, N. Maring, J. Senellart, and N. Belabas, *Optica* **11**, 427 (2024).
  - [35] A. Fyrrillas, N. Heurtel, S. Piacentini, N. Maring, J. Senellart, and N. Belabas, *arXiv preprint arXiv:2506.05988* (2025).
  - [36] R. Tang, R. Tanomura, T. Tanemura, and Y. Nakano, *ACS Photonics* **8**, 2074 (2021).
  - [37] Y.-L. Xiao, S. Li, G. Situ, and Z. You, *Optics and Lasers in Engineering* **139**, 106499 (2021).
  - [38] Y. Yang, R. J. Chapman, B. Haylock, F. Lenzini, Y. N. Joglekar, M. Lobino, and A. Peruzzo, *Nature Communications* **15**, 50 (2024).
  - [39] K. Zelaya, M. Honari-Latifpour, and M.-A. Miri, *npj Nanopho-*

- tonics **2**, 6 (2025).
- [40] S. Kuzmin, I. Dyakonov, and S. Kulik, Optics Express **29**, 38429 (2021).
  - [41] B. Bantysh, K. Katamadze, A. Chernyavskiy, and Y. Bogdanov, Optics Express **31**, 16729 (2023).
  - [42] C. Cai and J. Wang, Micromachines **13**, 10.3390/mi13040630 (2022).
  - [43] S. Rahimi-Keshari, M. A. Broome, R. Fickler, A. Fedrizzi, T. C. Ralph, and A. G. White, Optics express **21**, 13450 (2013).
  - [44] R. Heilmann, M. Gräfe, S. Nolte, and A. Szameit, Science bulletin **60**, 96 (2015).
  - [45] A. Abou Khalil, P. Lalanne, J.-P. Bérubé, Y. Petit, R. Vallée, and L. Canioni, Optics Express **27**, 31130 (2019).
  - [46] R. Sinkhorn and P. Knopp, Pacific Journal of Mathematics **21**, 343 (1967).
  - [47] A. Laing and J. L. O'Brien, arXiv preprint arXiv:1208.2868 (2012).
  - [48] D. Suess, N. Maraviglia, R. Kueng, A. Mañnos, C. Sparrow, T. Hashimoto, N. Matsuda, D. Gross, and A. Laing, arXiv preprint arXiv:2010.00517 (2020).
  - [49] B. C. Hall and B. C. Hall, *Lie groups, Lie algebras, and representations* (Springer, 2013).

## Appendix A: Fabrication process

The waveguide circuit was written using 515-nanometer laser pulses, which were the second harmonic of the Avesta Antaus ytterbium fiber femtosecond laser system. These pulses had a duration of 280 femtoseconds and were delivered at a repetition rate of 1 megahertz. Each pulse had an energy of 120 nanojoules and a linear polarisation parallel to the writing direction inside the fused silica glass sample. The laser beam was focused using an aspheric lens with a numerical aperture (NA) of approximately 0.55, 15 microns below the surface of the sample. A 150-micron-thick cover glass was placed between the lens and the sample to partially correct for spherical aberrations. A reconfigurable beam expander was used to enlarge the input aperture of the focusing lens. A high-precision AeroTech Fiber Glide 3D air-bearing system was used to move the sample at a speed of 0.2 mm/s during the waveguide fabrication process. The average propagation loss is approximately 0.65 dB/cm at 925 nm, and the coupling loss is approximately 1.5 dB per end face. Additionally, the bending loss was less than 0.1 dB/cm for a bending radius of 60 mm used in the experiment.

## Appendix B: Optical chip design

Our photonic processor contained an auxiliary part of three cascaded Mach-Zehnders' interferometers (MZIs) and a target  $4 \times 4$  interferometer consisting of two  $4 \times 4$  directional couplers and a phase shift layer in between. The design of the entire optical chip, including the waveguide structure and the electrode pattern, is shown in Fig. 5. The radius of curvature for almost all bends is 60 mm, which is a compromise between the bending loss effect and the overall size of the waveguide structure that can be achieved using our manufacturing process. The inner pair of waveguides in the  $4 \times 4$  directional

couplers have approximately three times larger radius of curvature. The input and output ports are spaced 250 microns apart and are connected to single-mode fiber optic arrays.

The thermo-optical phase shifters (or electrodes, or heaters) are fabricated using the same FSLW setup, with a very similar process to that used for writing waveguides. All the FSLW setup parameters for the thermo-optical phase shifters fabrication are identical, except for the sample translation speed, which is five times faster during the electrode engraving process (0.2 mm/s for waveguide writing and 1 mm/s for electrode engraving) to shorten the processing time. The FSLW setup for electrode engraving is less demanding, as we only need to remove metal from the border of the electrode. The laser power should be sufficient to engrave the electrode border. However, it should not be set too high, as it can damage the surface of the optical chip. Both these conditions are typically automatically met for the FSLW waveguide writing process, which is much more challenging to achieve and may require additional research [45]. In our fabrication process the thermo-optical phase shifters are engraved on a thin metallic film, which is sputtered after the waveguide structure of the interferometer has been written. The thermo-optical phase shifters must be precisely placed exactly above the corresponding waveguides. We ensure the electrode position by using special markers (blue dots in the Fig. 5a) previously inscribed underneath the surface in the corners of the fused silica substrate during the waveguide writing process. The thermo-optical phaseshifters are 35  $\mu\text{m}$  wide and 3.7 mm long metal stripes, which shape repeats the corresponding interferometer arm. The transverse spacing (perpendicular to the waveguide axis) between the heaters was 250  $\mu\text{m}$ . The NiCr 0.2  $\mu\text{m}$  thick film covers the whole surface of the chip, therefore in Fig. 5 all the white space is covered with metal, while the blue lines represent the engraved tracks, which isolate electrodes from each other. The electrodes are connected to a multi-channel digital computer controlled current source via a PCB interface with spring-loaded contacts, which contact points are schematically shown as red and black dots in Fig. 5a (each red dot corresponds to a single heater, whereas each black dot corresponds to a common round electrode). The resistances of all MZI heaters are approximately 1000  $\Omega$ , while the resistances of the target interferometers' heaters are 1700  $\Omega$ , as they have greater length. In the actual optical chip, two identical interferometric structures were fabricated in case one of them turned out to be unusable for some reason, or if more than two heaters corresponding to a particular interferometric arm were burned out.

## Appendix C: Preparation part calibration

The preparation part of our optical chip comprising of three cascaded MZIs can be calibrated with the help of the four parallel auxiliary waveguides, which couples the output waveguides of the preparation part of the chip as shown in Fig. 6. Therefore, to calibrate the three MZIs of the preparation part, we injected coherent laser radiation in the second input port of the chips' first (and main) floor of the waveguides and regis-



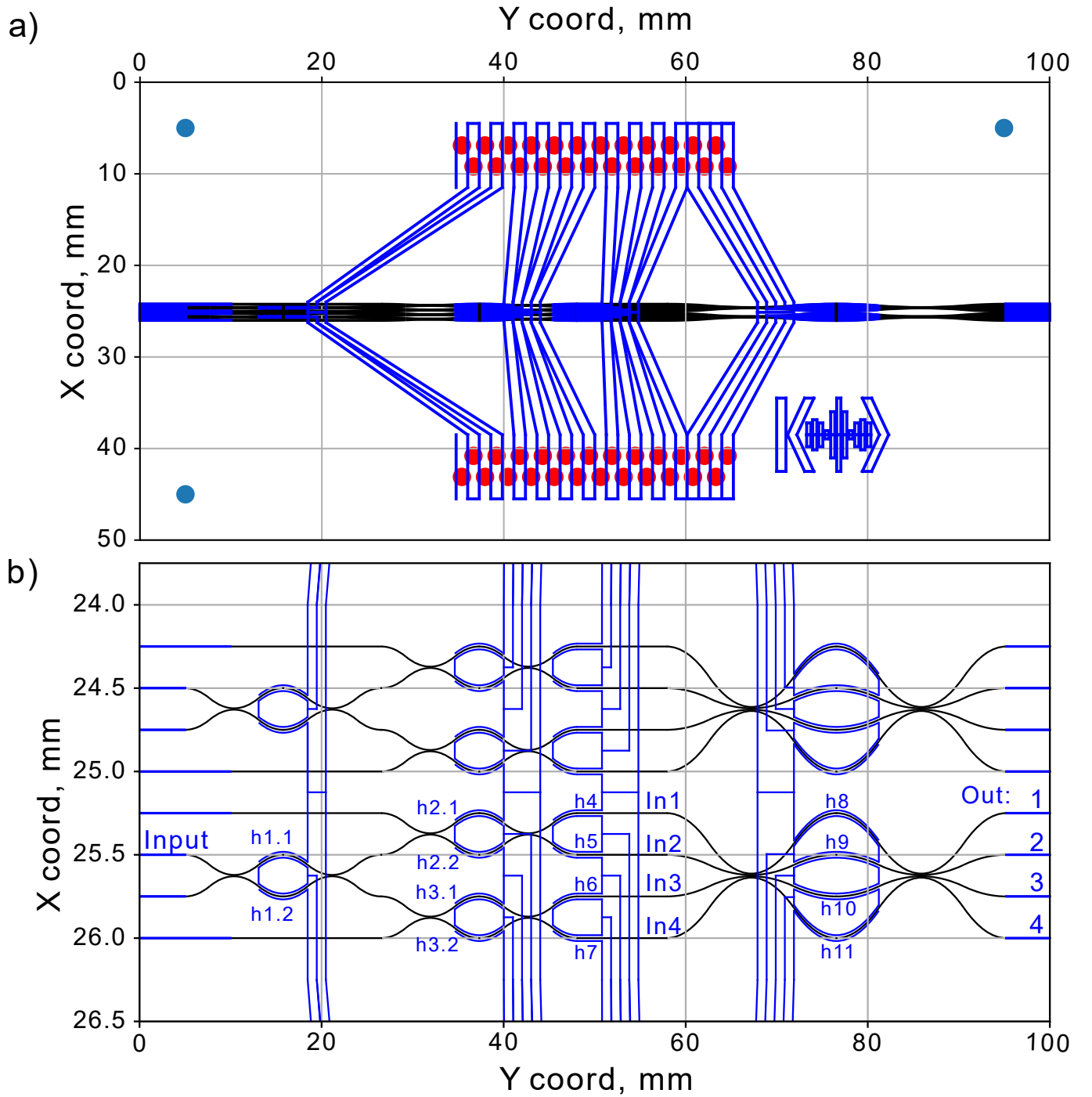


FIG. 5. The actual optical chip structure, viewed from the top. a) A real-scale schematic of chip. The red and black dots represent electrical and ground connections to the PCB, respectively, and the blue dots represent special markers on a fused silica sample, which are required for precise chip alignment before electrode engraving. b) Zoomed-in part of waveguide structure and electrodes. Waveguides are depicted by black solid lines, and engraved electrodes by solid blue lines. A thin metal film covers the entire top surface of the chip, meaning that the entire white area in the figure is conductive, whereas the blue lines represent isolation trenches between electrodes.

tered the output radiation from the output ports of the auxiliary waveguides - i.e. a second floor of the waveguide structure of our optical chip.

In practice, coherent radiation is injected into the chip, and the output radiation is collected from the chip using v-groove

fiber arrays placed on a six-axis micrometric positioner.

The optical power coupling between the preparation part of the interferometer and the auxiliary waveguides was deliberately made weak ( $\leq 10\%$ ) so as not to loosen much of the signal injected into the target interferometer. However,

the amount of coupled radiation was sufficient to calibrate the MZIs.

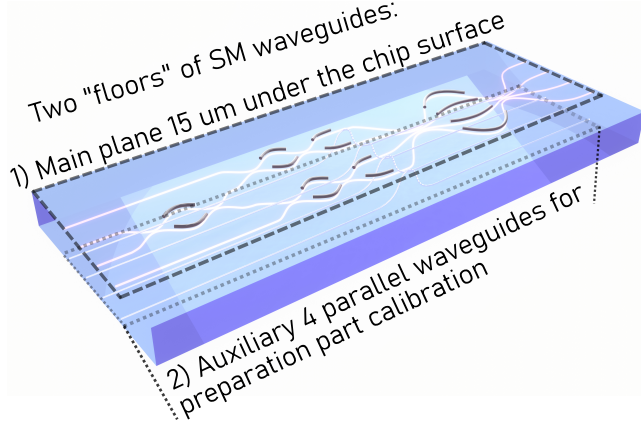


FIG. 6. Schematic picture of the optical chips' actual waveguide structure. Four auxiliary parallel waveguides were used to calibrate the preparation part of the optical chip. Each of 4 auxiliary parallel waveguides weakly couples the corresponding output waveguide of the preparation part of the optical chip, which is sufficient for the calibration of each of three MZIs for realizing an arbitrary input to the target interferometer.

#### Appendix D: Simultaneous approximation details

As stated in the main text, the necessary data for calibration of the phase shift layer is obtained by consequently injecting coherent radiation into each input port of the target interferometer and applying current in some range at each heater (at once) while measuring the optical power from all the output ports.

Calibration data were gathered as follows:

1. Coherent laser radiation at wavelength  $\lambda$  was injected in the  $k$ -th input mode of the target interferometer  $k \in \overline{1, 4}$  (see Fig. 1b).
2. Current was being applied to the heater  $j \in \overline{1, 3}$  in range from 0 to 15.6 mA with the step of 0.12 mA (resulting in 131 different current values), while the optical power was being measured from each  $m$ -th output port of the chip (see Fig. 1b). The measured optical power was then normalized.
3. The data then is organized in a way that allows each data point to be accessed using four indices: input port number  $k \in \overline{1, 4}$ , heater number  $j \in \overline{1, 3}$  at which current  $x$  was applied, index  $i \in \overline{1, 131}$  that enumerates the applied current  $x_i$  values ( $x_0 = 0$  mA and  $x_{131} = 15.6$  mA), and output port number  $m \in \overline{1, 3}$  (there is no  $m = 4$  as the output power was normalized  $\sum_m P_m = 1$  and therefore three independent output powers left).

$$P(k, j, i, m) = \left\{ \begin{array}{l} \text{Normed power from } m\text{-th output port,} \\ \text{while laser is injected in } k\text{-th input port} \\ \text{and current } x_i \text{ is applied at } j\text{-th heater} \end{array} \right\} \quad (\text{D1})$$

Therefore, the complete experimental data contain 4716 data points, as  $4 \text{ input ports} \times 3 \text{ heater} \times 3 \text{ normed output ports} \times 131 \text{ current values} = 4716$ . Each data point  $P_{exp}(k, j, i, m) \leq 1$  by construction.

An example of the experimentally measured complete calibration data for the wavelength  $\lambda = 925$  nm is depicted using dots in Fig. 8.

The digital model of chip  $U_{sim}$  can predict the normalized output optical power from the target interferometer corresponding to a concrete set of  $\{k, j, i, m\}$  indices:  $P_{sim}(k, j, i, m)$ . The main task of calibrating the phase shifts is to find a digital model of the target interferometer that approximates all experimentally measured data points  $P_{sim}(k, j, i, m) \approx P_{exp}(k, j, i, m)$ . This task is accomplished by optimization of parameters of the chips' model  $U_{sim}$  to maximize the  $R^2$  coefficient of determination (loss function) as follows:

$$R^2 = 1 - \frac{\sum_{k,j,i,m} (P_{exp}(k, j, i, m) - P_{sim}(k, j, i, m))^2}{\sum_{k,j,i,m} (P_{exp}(k, j, i, m) - \overline{P_{exp}})^2}, \quad (\text{D2})$$

where  $\overline{P_{exp}} = \frac{1}{N} \sum_{k,j,i,m} P_{exp}(k, j, i, m)$  and  $N$  is the total number of data points, which equals  $N = 4716$  in our experiment. Thus, the described optimization procedure is nothing but a curve fitting. Further, we need to determine 30 real parameters: 9 in each mode mixing matrix  $M_{1,2}$ , 3 bias zero phase shifts  $\Phi_0$  and 9 elements of the  $3 \times 3$  crosstalk matrix  $A = \{\alpha_{ij}\}$ . As the mode mixing matrices  $M_{1,2}$  were parameterized by a universal interferometer consisting of triangular meshes of MZIs, all optimization parameters except for nine  $\{\alpha_{ij}\}$  are phase shifts that can be varied in the  $[0, 2\pi]$  range. We have not supposed any apriori information about  $M_{1,2}$  form and treat them as two independent generally different unitary matrices parametrized by nine real parameters each ( $t_{1-9}$  and  $t_{10-18}$ ), whose initial values for optimization were chosen at random from  $[0, 2\pi]$ . The initial values for the bias phase shifts,  $\Phi_0$ , are always taken as zero. However, the initial guess for the nine crosstalk matrix elements  $\{\alpha_{ij}\}$  should have been chosen more accurately, both because it did not have finite bounds of its' values as phase shifts parameters  $t_j$  and  $\Phi_0$  had a  $[0, 2\pi]$ , and because it had an explicit physical meaning of thermal distribution in the sample material that must be governed by the geometry of the heaters and the heat equation. Therefore, a preliminary estimate of (at least) the relative values of the crosstalk matrix elements  $\{\alpha_{ij}\}$  is necessary.

To estimate the relations between crosstalk matrix elements  $\alpha_{ij}$  we considered a simple system of four equivalent (endless) straight and parallel heaters of width  $r_0$  that are placed above four equivalent (endless) straight and parallel waveguides spaced at a distance  $d$  apart from each other (see Fig.

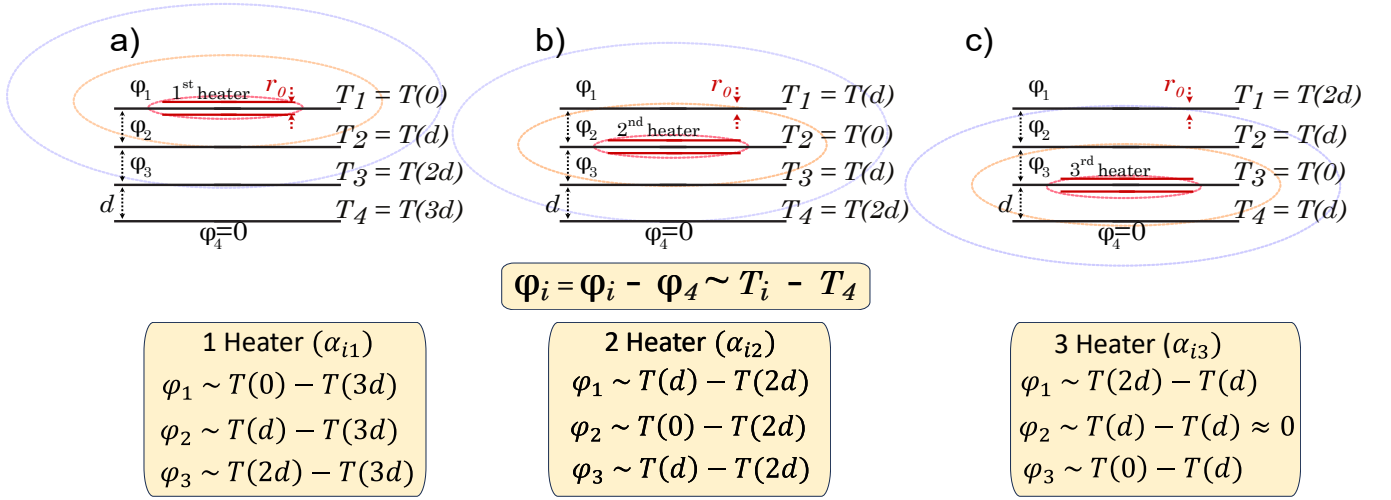


FIG. 7. Guidelines for the relative crosstalk estimation.

7). Such a model system, perhaps, roughly describes the heaters in our actual target interferometer which are notably not straight, as shown in Fig. 5b. Nevertheless, this simplified model can still be helpful for estimation.

The physical meaning of the crosstalk matrix  $A = \{a_{ij}\}$  is how "strong" the  $j$ -th heater affects the  $i$ -th heater (or, more precisely, the  $i$ -th interferometric arm). For example, if current  $x_1$  is applied to the first heater (see Fig. 7a) it will cause the phase shift change not only in the first waveguide  $\varphi_1(x_1)$ , on which it is supposed to affect, but in the second  $\varphi_2(x_1)$  and third  $\varphi_3(x_1)$  waveguides as well. However, the impact of the first heater on the second waveguide is lower than that on the first one, and the impact of the first heater on the third waveguide is even lower than that on the second one. This is because the phase shift induced by the heater is proportional to the temperature of the material in which the waveguide is embedded, and the temperature decreases with the distance from the thermal energy source.

The known geometry of the system can be used to quantitatively estimate the relations between  $a_{ij}$  values. Let the  $j$ -th heater receive some current  $x$ . We consider the logarithmic temperature decay with distance from the heater:

$$T(r) = \begin{cases} T_0, & |r| \leq r_0 \\ T_0 - \beta \ln \frac{r}{r_0}, & |r| > r_0, \end{cases} \quad (\text{D3})$$

where  $T_0$  is the maximum temperature of the heater, and  $\beta$  is a constant with the dimension of temperature. For the four waveguides in phase shift layer, three relative phase shifts are sufficient. We assume that all three phase shifts are relative to the fourth waveguide:  $\varphi_i \equiv \varphi_i - \varphi_4$  for  $i \in [1, 3]$ , which means  $\varphi_i$  is the phase shift between the  $i$ -th waveguide and the fourth waveguide (or  $\varphi_4 \equiv 0$ ). The phase shift  $\varphi_i$  arises because of the temperature difference between the  $i$ -th and fourth waveguides:  $\varphi_i - \varphi_4 \sim T_i - T_4$ . Therefore, when  $j$ -th heater receives some current  $x$  it leads to a phase shift  $\varphi_{ij}$  at  $i$ -th waveguide because of the temperature distribution in the

material, as follows:

$$\begin{array}{lll} \text{1st heater}(\alpha_{i1}) & \text{2nd heater}(\alpha_{i2}) & \text{3rd heater}(\alpha_{i3}) \\ \varphi_{11} \sim T(0) - T(3d) & \varphi_{12} \sim T(d) - T(2d) & \varphi_{13} \sim T(2d) - T(d) \\ \varphi_{21} \sim T(d) - T(3d) & \varphi_{22} \sim T(0) - T(2d) & \varphi_{23} \sim T(d) - T(d) \\ \varphi_{31} \sim T(2d) - T(3d) & \varphi_{32} \sim T(d) - T(2d) & \varphi_{33} \sim T(0) - T(d) \end{array} \quad (\text{D4})$$

, as shown schematically in Fig. 7. Without concretizing the explicit  $T(r)$  dependence, it immediately follows from (D4) that in the system with the simple geometry of parallel heaters,  $\varphi_{23} \approx 0$ , as the temperatures at the fourth and second waveguides are equal when current is applied to the third heater (which is due to the symmetry of the simplified system). Moreover, when the third heater was turned on, the temperature at the fourth waveguide was greater than that at the first, which led to the negativity of  $\varphi_{13} < 0$ . Other qualitative relations between induced phase shift  $\varphi_{ij}$  can be excluded from (D4) such as:  $\varphi_{11} > \varphi_{22} > \varphi_{33} > \varphi_{21} > \varphi_{12} \approx \varphi_{32} > \varphi_{31} > \varphi_{23} \approx 0 > \varphi_{13}$ , and  $|\varphi_{13}| \approx \varphi_{12}$ , which all follows from the fact that the temperature decreases with distance from the energy source.

The relations between the phase shifts  $\varphi_{ij}$  becomes quantitative after substituting the logarithmic law for the temperature in (D4):

$$\begin{array}{lll} \text{1st heater}(\alpha_{i1}) & \text{2nd heater}(\alpha_{i2}) & \text{3rd heater}(\alpha_{i3}) \\ \varphi_{11} \sim \beta \ln \frac{3d}{r_0} & \varphi_{12} \sim \beta \ln 2 & \varphi_{13} \sim -\beta \ln 2 \\ \varphi_{21} \sim \beta \ln 3 & \varphi_{22} \sim \beta \ln \frac{2d}{r_0} & \varphi_{23} \approx 0 \\ \varphi_{31} \sim \beta \ln \frac{3}{2} & \varphi_{32} \sim \beta \ln 2 & \varphi_{33} \sim \beta \ln \frac{d}{r_0} \end{array} \quad (\text{D5})$$

from which, after dividing everything by the constant  $\ln \frac{3}{2}$  the

crosstalk matrix  $A$  can be written as:

$$A_{model} = \alpha_0 \begin{pmatrix} \log_{1.5} \frac{3d}{r_0} & 1.71 & -1.71 \\ 2.71 & \log_{1.5} \frac{2d}{r_0} & 0 \\ 1 & 1.71 & \log_{1.5} \frac{d}{r_0} \end{pmatrix}, \quad (D6)$$

where  $1.71 = \log_{1.5} 2$  and  $2.71 = \log_{1.5} 3$ . As can be seen from (D6) relations between non diagonal elements of  $A$  are constant for any system of straight parallel heaters (and waveguides), whereas the diagonal elements of  $A$  are functions of a dimensionless parameter  $\xi = \frac{d}{r_0}$ .

To estimate the initial guess for the real crosstalk matrix  $A_{exp}$  describing the actual geometry of the heaters (see Fig. 5b) we substitute in (D6) the approximate value of  $\xi$  relevant for our device. In our target interferometer, the geometries of all heaters are arcs of a circle. The effective  $d_{exp}$  parameter of our actual chip can be taken as the average between the largest  $d_{max} = 250 \mu\text{m}$  in the centre of a phase shifts layer and the lowest  $d_{min} \approx 130 \mu\text{m}$  at the edges of the heaters, which gives  $d_{exp} \approx 190 \mu\text{m}$ . The heater width was the same for all the heaters of the chip and was equal to  $r_0 = 35 \mu\text{m}$ . Therefore, for  $\xi_{exp}$  we have  $\xi_{exp} = \frac{d_{exp}}{r_0} \approx 5.43$  resulting in an estimation of the initial guess for the crosstalk matrix  $A_{estim}$ :

$$A_{estim} = \alpha_0 \begin{pmatrix} 6.88 & 1.71 & -1.71 \\ 2.71 & 5.88 & 0 \\ 1 & 1.71 & 4.17 \end{pmatrix}, \quad (D7)$$

With (D7) as an initial guess for  $A$ , three zeros as a starting point for  $\Phi_0$  and 18 random numbers from  $[0, 2\pi]$  for  $M_{1,2}$ , we launched optimization, and it successfully converged to a value of coefficient of determinacy  $R^2 = 0.9972$  on 4716 data points. The predicted by the model output powers  $P_{sim}(k, j, i, m)$  and experimentally measured data points  $P_{exp}(k, j, i, m)$  are plotted in Fig. 8 as a curves and dots, respectively.

The successfully terminated optimizer returned the following values for  $A_{exp}$ :

$$A_{exp} = \alpha_0^{exp} \begin{pmatrix} 6.79 & 1.5 & -2.0 \\ 2.71 & 6.0 & -0.29 \\ 1 & 1.71 & 4.29 \end{pmatrix}. \quad (D8)$$

As we can see from the optimization experimental crosstalk matrix  $A_{exp}$  did not go too far from the initial estimation  $A_{estim}$ , which demonstrates the goodness of the simplified model used for the crosstalk  $A_{estim}$  estimation. Nevertheless, a qualitative difference between  $A_{exp}$  and  $A_{estim}$  can be observed which is a negative slightly non-zero  $\alpha_{23} < 0$ . However, this value can be legitimately explained by the actual geometry of the heaters and waveguides of our chip (see Fig. 5b). In fact, the distance between the third heater and the fourth waveguide is always slightly smaller (or equal at the centre) than the distance between the third heater and second waveguide, which results in higher temperatures at the fourth waveguide compared to the

second, leading to a negative phase shift in the second waveguide relative to the fourth.

No special assumptions on the bias (zero current) phase shift  $\Phi_0$  were made, and their initial guess values were set to zero  $\Phi_0^{init}$ . The Optimized values for  $\Phi_0^{exp}$  at a wavelength 925 nm appeared to be  $\Phi_0^{exp} = \{0.23, 0.98, 1.02\}$  rad. These values can also be explained by the actual geometry of the waveguides in the phase shift layer, as the first and fourth waveguides have the same length  $L_{1,4}$  and the second and third waveguides have the same length, which is clearly smaller than  $L_{1,4}$  (see Fig. 5b).

## Appendix E: Unitaries on chip measurement

Preparation interferometer which was consisted of three cascaded MZIs had the main purpose to serve as a tool on chip for stable and automated unitary transformation  $U$  of the target interferometer measurement. Measurement of the unitary matrix of the target interferometers was performed by exploiting coherent laser radiation according to [43].

The task of experimental measuring unitary matrix  $U_{ij} = |U_{ij}|e^{i\phi_{ij}}$  is to determine all its' modules  $|U_{ij}|$  and angles  $\phi_{ij}$ . Modules  $|U_{ij}|$  of the target unitary can be obtained simply by injecting the coherent laser radiation into each single input port of the target interferometer and then measuring the normalized power distribution from all output ports of the target interferometer:

$$|U_{ij}| = \sqrt{\frac{P_{ij}}{\sum_j P_{ij}}}, \quad (E1)$$

where  $P_{ij}$  is the measured optical power from the  $i$ -th output port of the interferometer, whereas radiation is injected solely into the  $j$ -th input port. By repeating this experimentally simple procedure  $N$  times for each input port of the target interferometer, a matrix of its modules  $|U_{ij}|$  can be obtained. However, despite the simplicity of such measurement, there is little subtlety in determining the modules  $|U_{ij}|$  of a linear optical interferometer. This arises from the possible presence of inhomogeneous losses at the output ports of the target interferometer, which would lead to the non unity sum of the absolute values squared of the matrix elements  $S_i^{row} = \sum_j |U_{ij}|^2 \neq 1$  that should sum to 1 for general unitary matrices. Whereas, all the columns sum to 1 by construction  $S_j^{col} = \sum_i |U_{ij}|^2 = 1$ . This inconsistency can be resolved by adjusting the matrix of squared modules  $|U_{ij}|^2$  multiplying it from both sides by a two diagonal matrices  $D_1$  and  $D_2$  with strictly positive elements, representing losses at input and output of the chip, such that new matrix  $|U_{ij}|_{new}^2$  satisfies the unitary requirements and all its' rows and all columns sum to 1. These matrices  $D_1$  and  $D_2$  can be found by a straightforward iterative method called the Sinkhorn–Knopp algorithm [46]. Therefore, this rescaling of the initially measured modules  $|U_{ij}|$  should be performed, if needed.

Angles  $\phi_{ij}$  can also be extracted from the optical power measurement by means of registering the interference that requires injecting coherent laser radiation into two input ports.



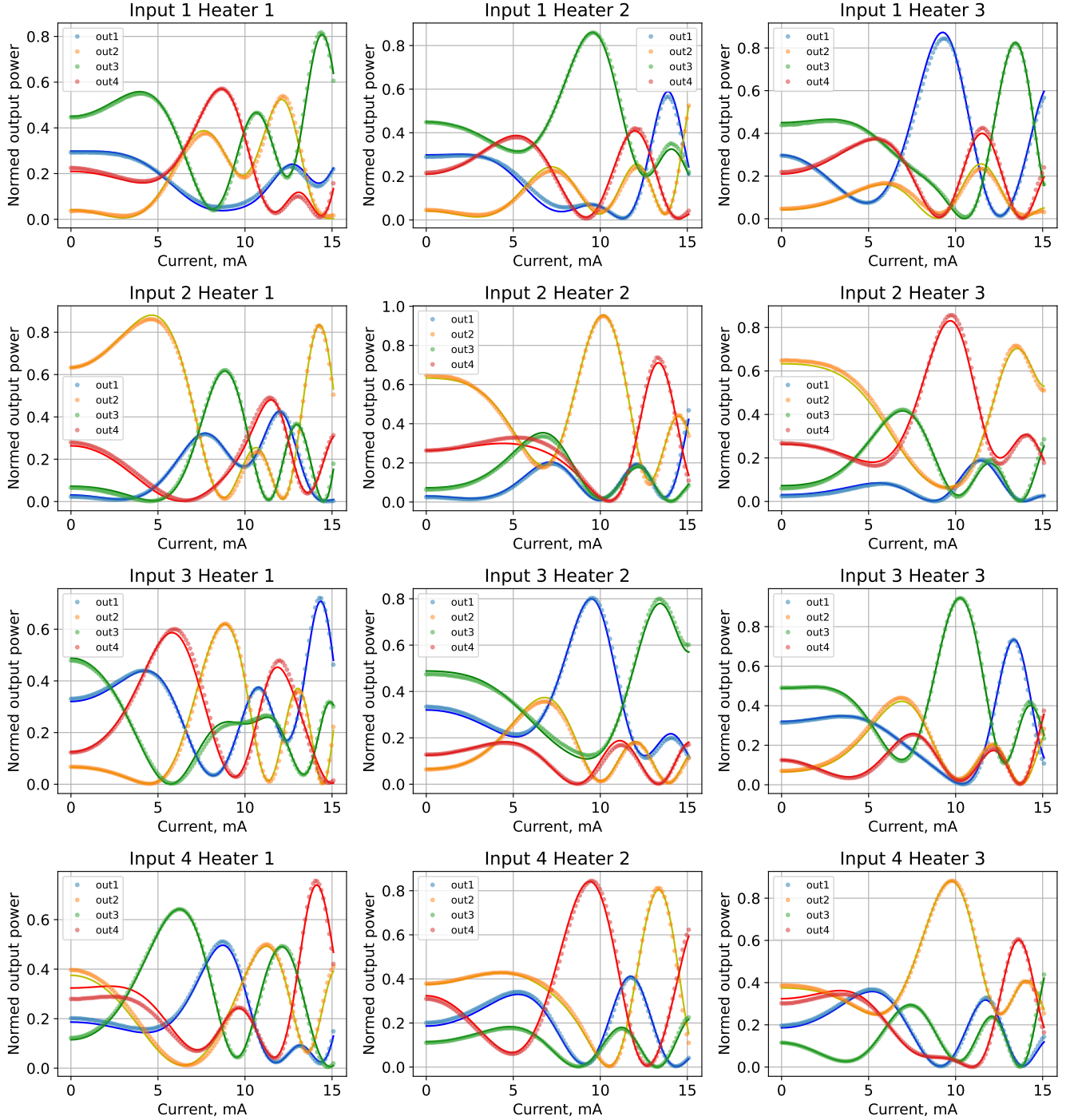


FIG. 8. Simultaneous approximation of all the experimental calibration data according to (5). The measured normed optical power from the corresponding output port is depicted with dots, and a simultaneous approximation curve is shown as lines with corresponding colours. The coefficient of determination between the experimental data points and the simulated values  $R^2 = 0.9972$ .

We assume that coherent radiation is injected into the  $l_1$  and  $l_2$  input ports of the target interferometer of the form

$$E_{in} = \{0, \dots, a, \dots, be^{i\theta}, \dots, 0\}^T, \quad (E2)$$

where  $a$  and  $be^{i\theta}$  are the complex amplitudes of the input co-

herent field such that  $a^2 + b^2 = 1$ . With no loss of generality let's assume  $a$  and  $b$  to be real. Therefore,  $\theta$  is their relative phase shift. Let us also introduce a parameter  $x$  that can control the value of  $\theta$ . This parameter plays a crucial role in the angles  $\phi_{ij}$  measuring, as in typical experiment coherent ra-

diation is being splitted in two beams, which are then being injected into the  $l_1$  and  $l_2$  input ports of the target interferometer. Then, to one of splitted beams an extra phase shift  $\theta(x)$  is being added by varying the experimental parameter  $x$  and the output optical power distribution  $P(x)$  among output ports of the target interferometer is being measured. The angles of the  $l_2$  column of the target matrix  $\varphi_{il_2}$  can be extracted from the measured power from  $x$  curves  $P_k^{l_1, l_2}(x)$ . To determine angles in all other columns, usually  $l_2$  is being varied from 1 to  $N$  except for  $l_2 \neq l_1$ , while  $l_1$  is being fixed.

It can be shown that while radiation is being injected into  $l_1$  and  $l_2$  input ports, the optical power from the  $k$ -th output port of the target interferometer as a function of  $x$  is governed by:

$$P_k^{l_1, l_2}(x) = C_{l_1, l_2} + D_{l_1, l_2} \cos(\theta(x) + \varphi_{kl_2}), \quad (\text{E3})$$

where  $C_{l_1, l_2}$  and  $D_{l_1, l_2}$  are some constants (depending on the modulus of  $U$ ). It should be noted that in (E3) all angles in  $l_1$ -th column of the  $U$  matrix were assumed to be zero ( $\varphi_{kl_1} \equiv 0$  for each  $k \in \overline{1, N}$ ), as they can be associated with irrelevant  $N$  phase shifts  $P_{out}(\varphi_{kl_1})$  following after the target interferometer  $\tilde{U} \equiv P_{out}(\varphi_{kl_1}) \times U$  [43].

Then, after obtaining the experimental curves  $P(x)$  they can be approximated according to (E3) and the necessary angles  $\varphi_{kl_2}$  can be determined for each  $k \in \overline{1, N}$  and each  $kl_2 \in \overline{1, N-1}$  ( $l_2$  varies from 1 to  $N-1$  because  $l_2$  is a number corresponding to one of the two irradiated input ports of the target interferometer, and the other is  $l_1$ ).

We realized the procedure described above on a chip with the help of a preparation interferometer that can prepare any desired coherent input state to be sent to the target interferometer, including those of the form (E2). For angles measurement of the unitary  $U$  we used thermo-optical heaters at the output of the preparation part. Therefore, in our case, the current served as the  $x$  parameter and  $\theta(x) = \theta_0 + \alpha_\theta x^2$  leading to the  $P_k^{l_1, l_2}(x)$  dependence of the form:

$$P_k^{l_1, l_2}(x) = C_{l_1, l_2} + D_{l_1, l_2} \cos(\alpha_\theta x^2 + \gamma_{kl_2}), \quad (\text{E4})$$

where  $\gamma_{kl_2} = (\theta_0^{l_1, l_2} + \varphi_{kl_2})$ .

Therefore, to determine the angles of the unitary transformation of the target interferometer, we measured all the necessary  $P_k^{l_1, l_2}(x)$  curves and approximated each using (E4), which returns the values of the corresponding shifts in the sines angles  $\gamma_{kl_2}$ . For a fixed  $l_1$  and  $l_2$  each obtained angle  $\gamma_{kl_2}$  has the extra  $\theta_0^{l_1, l_2}$  term, which can be eliminated by subtraction the  $\varphi_{l_1 l_2}$  angle from each obtained  $\gamma_{kl_2}$  having ( $\tilde{\gamma}_{kl_2} = \gamma_{kl_2} - \varphi_{l_1 l_2}$ ) for each  $k \in \overline{1, 4}$  and each  $l_2 \in \overline{1, 4}, l_2 \neq l_1$ .

Eventually, the procedure of the target unitary  $U$  reconstruction results in an experimentally determined matrices of modules  $|U_{ij}|$  and angles  $\tilde{\gamma}_{ij}$ . The unitary matrix  $\tilde{U}_{ij}$  of interest is constructed using element-wise matrix multiplication as follows:

$$\tilde{U}_{ij} = |U_{ij}| \cdot e^{i\tilde{\gamma}_{ij}}, \quad (\text{E5})$$

where  $2N - 1 = 7$  values of  $\tilde{\gamma}_{ij}$  have zero values by construction. These are the angles of the  $l_1$ -th column and  $l_1$ -th row

of the reconstructed matrix  $\tilde{U}$  on the chip. The fact that in the reconstructed unitary transformation  $\tilde{U}$  of the target  $N$ -port interferometer,  $2N - 1$  angles are set to be real is inherent to any tomography algorithm [43, 44, 47, 48]. This is because of the physical equivalence of  $U$  and  $\tilde{U} = P_{out}(\vec{\varphi}_{out}) \times U \times P_{in}(\vec{\varphi}_{in})$ , where  $P_{in}(\vec{\varphi}_{in})$  and  $P_{out}(\vec{\varphi}_{out})$  are diagonal matrices with pure phases  $\vec{\varphi}_{in}$  and  $\vec{\varphi}_{out}$ , respectively. In other words, any tomography algorithm can reconstruct the unitary transformation of a linear optical interferometer only up to the input and output phases [43, 44, 47, 48].

As a final remark on the reconstruction procedure, the modules and angles measurements are conducted completely independently, which leaves no guarantee that the reconstructed by (E5) matrix  $\tilde{U}$  is unitary. Even in case if one had performed the Sinkhorn Knopp algorithm [46] to rescale the experimentally measured modules of  $\tilde{U}$ , the angles were still obtained using a separate interferometric procedure. However, if  $\tilde{U}$  appeared to be a non unitary, it can be projected to the closest matrix from the unitary subspace by, for example, polar decomposition or single value decomposition [49].

As, typically, optical power from the all output ports of the chip is being collected simultaneously each port by each photodetector, the number of separate measurements necessary for obtaining the modules  $|U_{ij}|$  for an  $N \times N$ -port interferometer is equal to  $N$ . Whereas the angles  $\tilde{\gamma}_{ij}$  measurement requires  $N - 1$  separate interference collections, resulting in  $2N - 1$  total number of measurements for the target  $N \times N$  unitary reconstruction.

In our experiment, we set  $l_1 = 1$  for every measurement of  $\tilde{U}$  on the chip, which causes the first row and first column of any measured  $\tilde{U}$  to be strictly real. However, because the measured unitary matrix of the target interferometer  $\tilde{U}$  is always in the form of a real first row and first column, the simulated  $U_{sim}$  matrix, generated by the chips' digital model, should be converted to this same form before their comparison, as the matrix fidelity (9) measure is sensitive to such deviations, while these unitaries are physically equivalent. This type of unitary matrix  $U_{sim} = \rho_{ij} \exp(i\varphi_{ij})$  transformation can easily be performed by multiplying it on both sides by diagonal unitary matrices:

$$\tilde{U}_{sim} = \Gamma \times U_{sim} \times \Omega, \quad (\text{E6})$$

where  $\Gamma = \text{diag}(e^{i\gamma_j})$  and  $\Omega = \text{diag}(e^{i\omega_i})$ , the elements of which are equal to  $\gamma_j = -\varphi_{1j} + \varphi_{11}$  and  $\omega_i = -\varphi_{i1}$ . After multiplying by  $\Gamma$  and  $\Omega$  unitary matrix  $U_{sim}$  transforms to  $\tilde{U}_{sim} = \rho_{ij} \exp(i\tilde{\varphi}_{ij})$  with zero angles in the first row and first column by construction:  $\tilde{\varphi}_{1j} \equiv \tilde{\varphi}_{i1} \equiv 0$ .

More generally, any  $N \times N$  unitary matrix  $U_{ij} = \rho_{ij} \exp(i\varphi_{ij})$  can always be multiplied on both sides by a diagonal  $N \times N$  unitary matrices  $\Gamma = \text{diag}(e^{i\gamma_j})$  and  $\Omega = \text{diag}(e^{i\omega_i})$  with appropriate angles  $\gamma_j$  and  $\omega_i$  such that the resulting unitary matrix  $\tilde{U}_{ij} = \rho_{ij} \exp(i\tilde{\varphi}_{ij})$  has purely real  $I$ -th row and  $J$ -th column:  $\tilde{\varphi}_{iJ} \equiv \tilde{\varphi}_{IJ} \equiv 0$ . The necessary angles,  $\gamma_j$  and  $\omega_i$  are obtained from:

$$\omega_i = -\varphi_{iJ}, \quad \gamma_j = -\varphi_{IJ} + \varphi_{IJ}. \quad (\text{E7})$$

We call this operation *the real border* the unitary matrix and define a *real border* function  $f_{rb}(U, I, J)$  that takes a unitary matrix  $U$  at its' input and returns another unitary matrix  $\tilde{U}$  with a purely real  $I$ -th row and  $J$ -th column.

Therefore, before calculating the matrix fidelity function (9) between the experimentally measured unitary transformation of the chip  $U_{exp}$  and the corresponding matrix  $U_{sim}$  simulated by the chips' digital model, both should be equivalently *real bordered*. All matrix fidelities shown in the histogram in Fig. 4a were calculated between appropriately *real bordered* pairs of  $U_{exp}$  and  $U_{sim}$ .

## Appendix F: Broadband optical switching details

Optical switches were realized via the chips' model at several wavelengths ranging from 915 to 975 nm. At each wavelength, the digital chip model was reconstructed using the calibration method. The reconstructed mode mixing matrices  $M_{1,2}$ , bias phase shift vectors  $\vec{\Phi}_0$  and crosstalk matrices  $A$  for each wavelength are shown in Fig. 11.

As shown in Fig. 11 the mode mixing matrices  $M_{1,2}^\lambda$  are slightly different for each wavelength  $\lambda$  preserving the property  $M_1^\lambda \approx M_2^\lambda$ . The bias phase shift vectors  $\vec{\Phi}_0$  varies with wavelength  $\lambda$  more significantly, but always in accordance with the actual geometry of the target interferometer:  $\varphi_1^\lambda \approx 0$  and  $\varphi_2^\lambda \approx \varphi_3^\lambda$  as discussed in Appendix D. Meanwhile, the crosstalk matrices  $A^\lambda$  for each wavelength  $\lambda$  are approximately the same. This is because the crosstalk matrix  $A$  describes the physical heaters (and is completely determined by them) and not the coherent radiation.

The necessary three phase shifts for implementing a particular port-to-port optical switch were obtained by an optimization procedure run on a standard PC (Python scipy.minimize method). Once the required phase shifts were determined from the digital model of the optical chip, they were applied to the actual device. Coherent radiation of a given wavelength was injected into the specific input port of the device. The optical power distribution at the output ports was then measured using photodiodes and compared with the target values. A comparison between the switching matrices  $U$  and  $V$  was performed according to the variation in the amplitude fidelity measure:

$$F_{ampl}^{(2)}(U, V) = \frac{\sum_{i,j} |u_{ij} v_{ij}|}{\sqrt{\sum_{i,j} |u_{ij} u_{ij}| \sum_{i,j} |v_{ij} v_{ij}|}} \quad (F1)$$

An example simulating coherent light with a wavelength of 975 nanometers propagating through a target interferometer, illustrating all possible port-to-port optical switch configurations, is shown in Fig. 12.

## Appendix G: Scaling of the proposed calibration procedure

The scalability of the proposed approach for programming a reconfigurable integrated interferometer is a crucial consid-

eration that needs to be carefully addressed. First, in our experiment, the tunable  $4 \times 4$  integrated interferometer consists of two passive mode mixing blocks  $M_{1,2}$  and an active phase shift layer  $P_1(\vec{\Phi}_1)$  between them. The phase shift layer consists of three thermo phase shifters. Therefore, our optical chip has only three tunable parameters and cannot be considered a  $4 \times 4$  universal photonic device. However, if two additional phase shift layers  $P_2(\vec{\Phi}_2)$  and  $P_3(\vec{\Phi}_3)$  were cascaded between the two additional constant mode mixing blocks  $M_3$  and  $M_4$  and added to our device, the resulting interferometer would become a  $4 \times 4$  universal interferometer [9, 10, 31].

The three-phase shift layer interferometer can be described as follows:

$$U(\vec{\Phi}) = M_4 \times P_3(\vec{\Phi}_3) \times M_3 \times P_2(\vec{\Phi}_2) \times M_2 \times P_1(\vec{\Phi}_1) \times M_1, \quad (G1)$$

where  $\vec{\Phi}_1 = \{\varphi_1, \varphi_2, \varphi_3\}$ ,  $\vec{\Phi}_2 = \{\varphi_4, \varphi_5, \varphi_6\}$  and  $\vec{\Phi}_3 = \{\varphi_7, \varphi_8, \varphi_9\}$ . The procedure for programming a universal interferometer with three-phase shift layers (G1) is similar to that of a single-phase shift layer device, except that a calibration routine must be performed three times for each phase shift layer  $P_{1,2,3}$ . Each calibration measurement will provide not only the phases of the current dependencies (including all crosstalk), but also information about each mode mixing block  $M_{1,2,3,4}$ .

To better understand how a complete digital model of an optical chip can be created from subsequent calibration measurements, let us consider an interferometer with two phase shift layers as an example (see Fig. 9a):

$$U(\vec{\Phi}) = M_3 \times P_2(\vec{\Phi}_2) \times M_2 \times P_1(\vec{\Phi}_1) \times M_1. \quad (G2)$$

Typically, the phase shift crosstalk between different phase shift layers is negligible, as these layers are located far enough apart from each other compared to the distance between the heaters within one phase shift layer. Therefore, each phase shift layer can be calibrated independently. The calibration of the first phase shift layer results in an optical chip model:

$$U(\vec{X}_1) = \underbrace{M_3 \times P_2(\vec{\Phi}_2^{(0)}) \times M_2}_{\tilde{M}_2 = \text{const}} \times P_1(\vec{\Phi}_1(\vec{X}_1)) \times M_1. \quad (G3)$$

This calibration will result in the exact phase from the current dependence for the first phase shift layer, as well as in the explicit form of the first mode mixing block  $M_1$  and effective mode mixing block  $M_2$ :

$$\tilde{M}_2 = M_3 \times P_2(\vec{\Phi}_2^{(0)}) \times M_2,$$

which implicitly contains the information about the actual  $M_2$ . Similarly, the calibration of the second phase shift layer results in an optical chip model:

$$U(\vec{X}_2) = M_3 \times P_2(\vec{\Phi}_2(\vec{X}_2)) \times \underbrace{M_2 \times P_1(\vec{\Phi}_1^{(0)}) \times M_1}_{\tilde{M}_1 = \text{const}}. \quad (G4)$$

This calibration will result in the exact phase from the current dependence for the second phase shift layer, as well as in the

explicit form of the third mode mixing block  $M_3$  and effective mode mixing block  $\tilde{M}_1$ :

$$\tilde{M}_1 = M_2 \times P_1(\vec{\varphi}_1^{(0)}) \times M_1,$$

which, again, just as  $\tilde{M}_2$  implicitly contains the information about the actual  $M_2$ . However, we know the explicit forms of  $M_1$  and  $P_1(\vec{\varphi}_1^{(0)})$  (which is the first phase shift layer with zero currents). This enables us to determine the actual second mode mixing block  $M_2$  as follows:

$$M_2 = \tilde{M}_1 \times M_1^{-1} \times (P_1^{(0)})^{-1}. \quad (\text{G5})$$

Moreover, the second mode mixing block  $M_2$  can also be independently obtained from  $\tilde{M}_2$ :

$$M_2 = (P_2^{(0)})^{-1} \times M_3^{-1} \times \tilde{M}_2. \quad (\text{G6})$$

The expressions (G5) and (G6) for calculating the  $M_2$  are independent, as entities  $M_1$ ,  $P_1^{(0)}$ ,  $\tilde{M}_2$  and  $M_3$ ,  $P_2^{(0)}$ ,  $\tilde{M}_1$  were obtained from two independent experimental calibration procedures for the first (G3) and second (G4) phase shift layers  $P_1(\vec{\varphi}_1(\vec{X}_1))$  and  $P_2(\vec{\varphi}_2(\vec{X}_2))$ , respectively. The two independent evaluations of  $M_2$  must be equivalent and can be used to validate the entire optical chip digital model. Figure 9 schematically illustrates the procedure described above for programming an interferometer with two phase shift layers.

Therefore, calibrating the interferometer with a similar (complex) waveguide structure, but with  $m$  phase shift layers instead of just one, would require performing  $m$  separate calibration procedures for each phase shift layer as described in this paper. Such a set of measurements would be sufficient for complete characterization and programming of the optical chip.

The required number of measurements for calibrating phase shift layer in a general  $N \times N$  interferometer is  $N$  input ports  $\times N - 1$  heaters, which is quadratic with respect to the number of modes. The number of real parameters required for optimization is also quadratic in the number of modes.

In other words, there are two ways to scale an interferometer: by increasing its length, or by increasing the width or the number of modes it contains. The first method is simpler and involves a linear increase in the number of measurements and amount of processing required. However, scaling by increasing the number of modes grows quadratically with both the number of measurements and parameters of the model that need to be optimized.

While the number of measurements cannot be decreased by increasing the number of modes,  $N$ , the number of parameters in the model can be reduced by carefully adjusting the model. Therefore, finding possible methods to reduce the number of model parameters is of great importance. For example, using prior knowledge of the structure of actual interferometers and the geometry of their waveguides can help reduce the number of parameters in the model. For instance, we used a physically inspired parametrization of the mode mixing matrices  $M_{1,2}$  in the form of coupled waveguide lattices, which required only four real parameters per matrix, instead of nine,

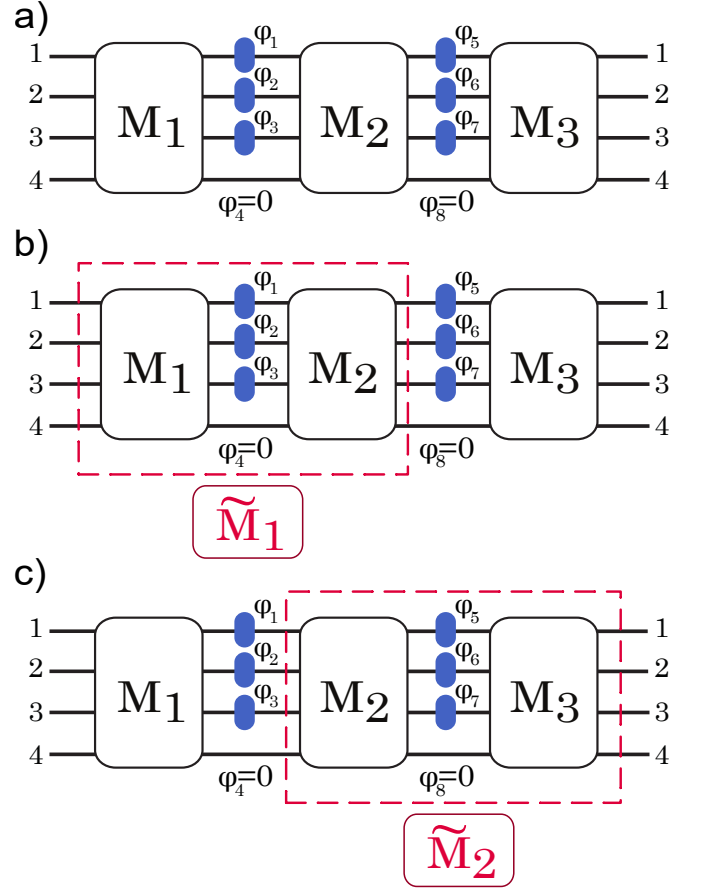


FIG. 9. A model of an interferometer with two phase shift layers and three mode mixing layers can be consequently treated as a) interferometer with one phase shift layer cascaded between two mode mixing layers and b) interferometer with one phase shift layer cascaded between two mode mixing layers. The mode mixing block,  $M_2$  can be implicitly determined.

for the universal triangular MZI mesh parametrization. With this parametrization of  $M_{1,2}$  and the same parametrization of the phase shift matrix, the total number of real parameters in our model is reduced from 30 to 20, which makes it significantly easier for the optimizer to find the optimal solution.

Technological advancements will also reduce the complexity of digital models. For example, the manufacturing of thermal phase shifters without mutual cross-interference eliminates all non-diagonal parameters  $\alpha_{ij}$  from the crosstalk matrix  $A$ , resulting in  $N - 1$  real parameters, which are the diagonal elements of  $A$ , instead of  $N - 1 \times N - 1$  for  $A$  with all nonzero elements. Alternatively, heaters can be designed to be straight and long relative to their width in order to simplify the model (7) of the phase shift layer with only two independent parameters (D6),  $\alpha_0$  and  $\xi = d/r_0$ , rather than  $N - 1 \times N - 1$  values of  $\alpha_{ij}$  (see Appendix D).



## Appendix H: Machine learning based method for chip programming

We also performed the learning of an artificial neural network on unitary matrices  $U_{exp}$  measured on chip to reconstruct the mode mixing layers  $M_{1,2}$  according to [40].

Both training and validation data sets unitaries, respectively, were taken from previously measured unitary matrices on the chip (see Fig. 4a). Learning was performed both on phase shifts - matrices dataset and currents - matrices dataset.

### 1. Phase shifts-matrices ( $\vec{\phi}$ - $U$ ) dataset

The dataset contained 27 pairs of unitary matrices and corresponding phase shifts  $\vec{\phi}$  obtained from the experimental calibration. This means that in such a dataset, we have knowledge of the phase shifts  $\vec{\phi}$  which were set on the chip and the corresponding measured unitary transformation  $U_{data}(\vec{\phi})$  of the chip. The neural network was trained on 27 unitary matrices for which the fidelity between them and the calibration model is greater than 0.95 (see Fig. 4a) and tested on the other 65 measured unitary matrices.

The trained model was:

$$U_{trained}(\vec{p}) = f_{rb}(A_2(\vec{p}_2) \times P(\vec{\phi}) \times A_1(\vec{p}_1)), \quad (H1)$$

where  $f_{rb}(\cdot)$  is a *real border* function defined in Appendix D,  $A_{1,2}$  is two arbitrary complex matrices (not necessarily unitary), and  $P(\vec{\phi}) = \text{diag}(e^{i\phi_1}, e^{i\phi_2}, e^{i\phi_3}, 1)$  is a diagonal phase shift matrix. Matrices  $A_{1,2}$  were considered to be general complex valued  $4 \times 4$  matrices and were parametrized by  $2 \times 4^2 = 32$  real parameters  $\vec{p}$  each, which represent element wise parametrization of real and imaginary parts of  $A_{1,2}$ . The initial values of  $\vec{p}$  were chosen randomly for each optimization run.

We used the Adaptive Moment Estimation optimization algorithm (Adam) on 5000 epochs with mini batches containing 5 random elements each. The Frobenius metric was chosen as the loss function, as in [40].

The results are presented in Fig. 10a. As can be seen from the results, the fidelity between the measured unitary matrices and predicted by the ML model is no less than 0.90 with a peak around 0.99, which indicates the accuracy of the revealed ML-based optical chip model. However, the phase shifts - matrices dataset require the knowledge of phase shifts information, which is obtained from the calibration procedure that provides the mode mixing elements  $M_{1,2}$  itself. Therefore, performing another optimization procedure to determine the  $A_{1,2}$  matrices, while already having the  $M_{1,2}$  may seem somewhat redundant. In this regard, a more fundamental dataset of currents and corresponding unitary matrices for chips' transformation is in high demand.

### 2. Currents-matrices ( $\vec{x}$ - $U$ ) dataset

The dataset contained 60 pairs of unitary matrices and the corresponding currents  $\vec{x}$  set on the chip. Such scenario has

more practical importance than the  $\vec{\phi}$ - $U$  dataset, as it contains solely primal raw data without any previous processing of it like calibration routine.

The neural network was trained on 60 random unitaries from measured matrices on chip (see Fig. 4a) and tested on the other 36 measured unitary matrices. In contrast to  $\vec{\phi}$ - $U$  dataset in  $\vec{x}$ - $U$  dataset, we assume no calibration  $\phi(x)$  information and hence cannot choose 60 unitaries with calibration model fidelity greater than 0.95 as in the previous subsection.

The trained model was:

$$U_{trained}(\vec{p}) = f_{rb}(A_2(\vec{p}_2) \times P(\vec{x}) \times A_1(\vec{p}_1)), \quad (H2)$$

where  $f_{rb}(\cdot)$  is a *real border* function,  $A_{1,2}$  is two arbitrary complex matrices (not necessarily unitary), and  $P(\vec{x}) = \text{diag}(e^{i\phi_1(\vec{x})}, e^{i\phi_2(\vec{x})}, e^{i\phi_3(\vec{x})}, 1)$  is a diagonal phase shift matrix with phase shifts from current dependence (7), resulting in 12 real parameters: 3 bias phase shifts  $\vec{\phi}_0$  and 9 crosstalk matrix  $A$  elements. Matrices  $A_{1,2}$  were again considered to be general complex valued  $4 \times 4$  matrices and were parametrized by 32 real parameters. The initial values for  $\vec{p}$  were chosen at random for each optimization run, while an initial guess for the crosstalk matrix  $\{\alpha_{ij}\}$  elements was taken according to the estimations discussed in the previous section (see Appendix D).

To train the network, the Adaptive Moment Estimation optimization algorithm was used on 6000 epochs with mini batches containing 5 random elements each. The Frobenius metric was chosen as the loss function as in [40].

The results are presented in Fig. 10b. As can be seen from the results, the fidelity between the measured unitary matrices and predicted by the trained ML model has a peak around 0.99; however, some points are less than 0.90, which proves the accuracy of the revealed ML-based optical chip model.

It is worth mentioning that in this experiment, training the artificial network on a currents-matrices ( $\vec{x}$ - $U$ ) dataset to determine the ML-based optical chip model (H2) aims to solve exactly the same task as the calibration of the phase shift layer. Both methods return the digital chip model as a function of the experimentally tunable parameters: electrical currents  $\vec{x}$ . This model enables the prediction of the unitary transformation of the chip at a given currents. However, despite sharing the same goal, these two methods differ in the experimental data they utilize. The calibration method requires all the output power from the current dependencies, whereas the ML method requires a set of unitary matrices measured on the chip. Under realistic experimental conditions, it may not always be easy to perform full optical chip tomography, in contrast to simple output power calibration measurements. At least, because if we use the same experimental resources (coherent laser radiation), full chip tomography would require injecting the radiation into two ports of the chip simultaneously and precisely varying their relative phase shift. However, only one input port was used in the calibration measurements. Both methods then use optimization over a set of real-valued parameters to minimize the corresponding loss function.

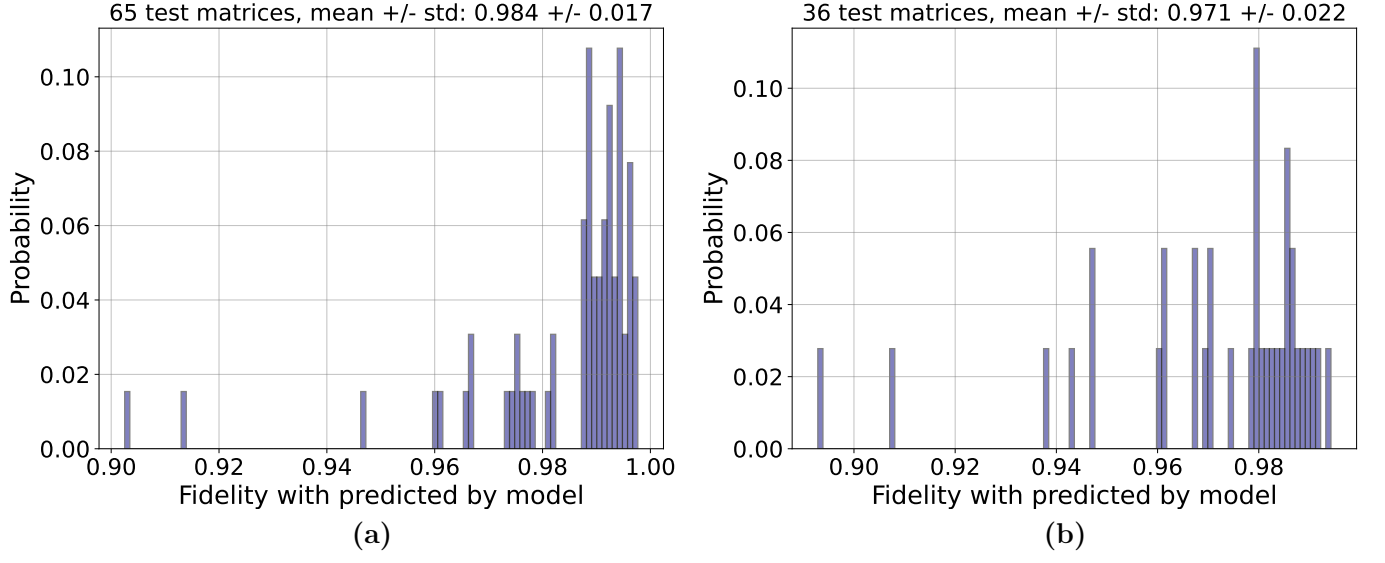


FIG. 10. The fidelity distribution histograms for ML based model test. a) Testing the learning of artificial neural network on phase shifts-matrices ( $\vec{\phi}-U$ ) dataset. b) Testing the learning of artificial neural network on currents-matrices ( $\vec{x}-U$ ) dataset.

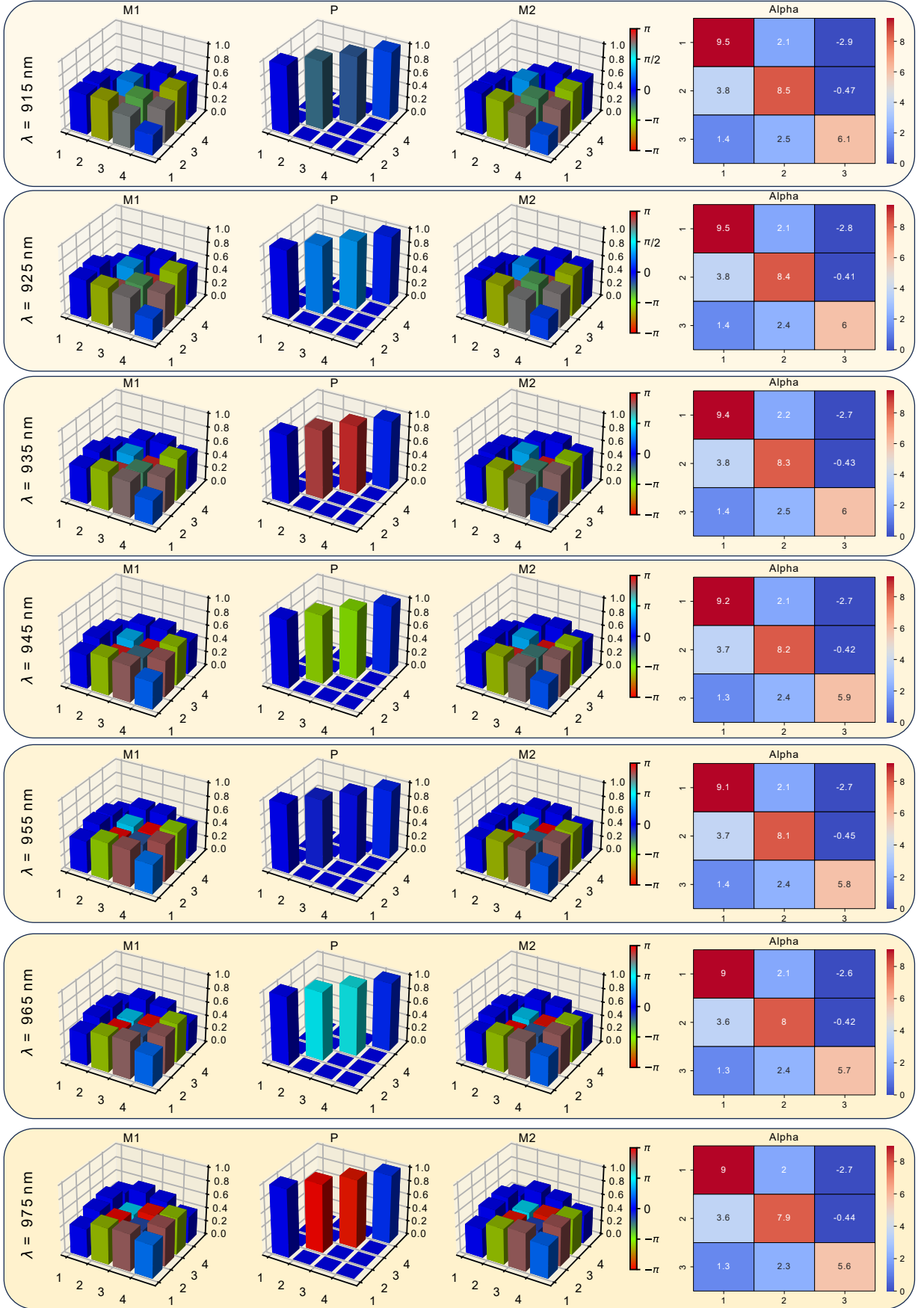


FIG. 11. The reconstructed mode mixing matrices  $M_{1,2}$ , bias phase shift vectors  $\vec{\Phi}_0$  and crosstalk matrices  $A$  for each wavelength from 915 to 975 nm

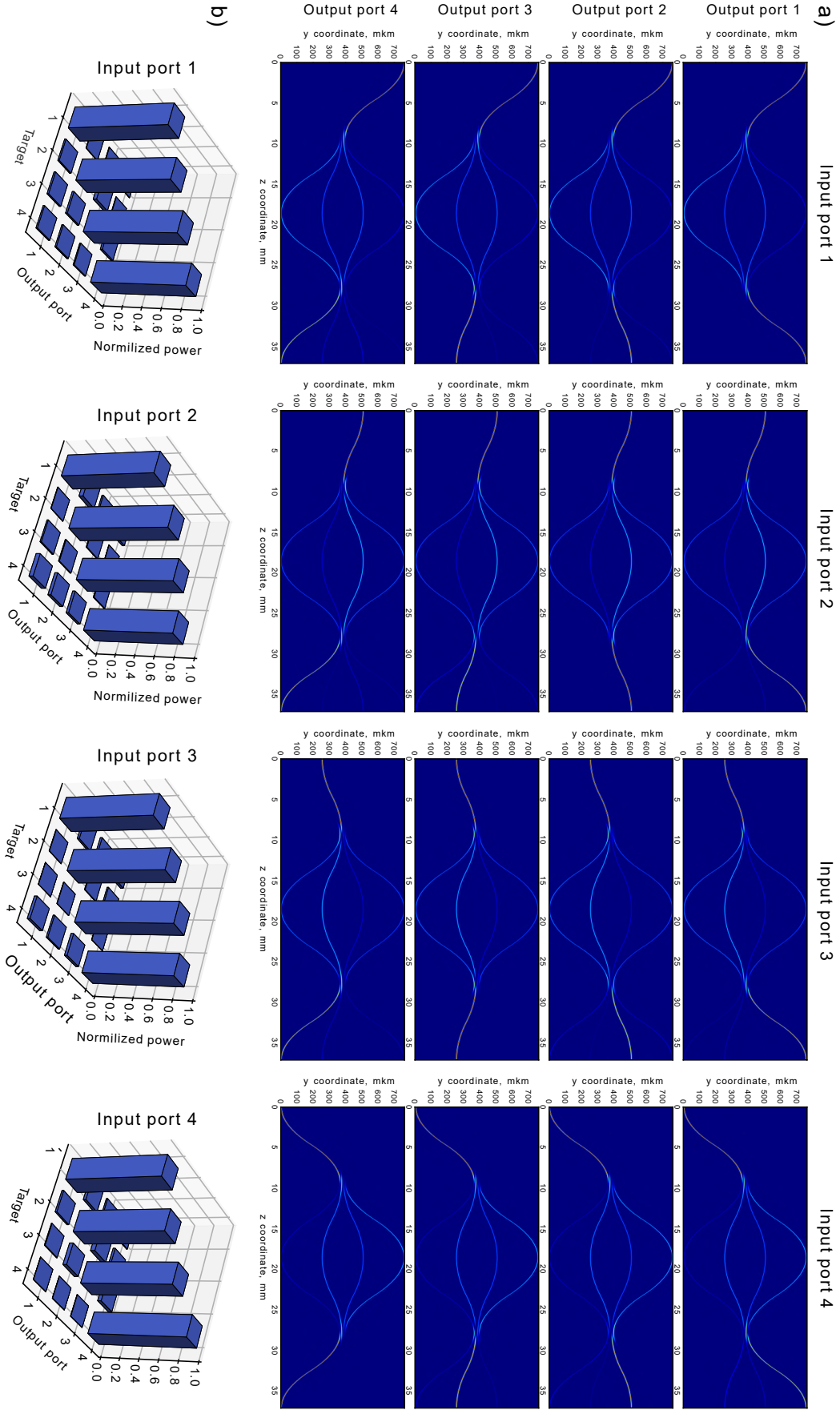


FIG. 12. a) Visualization of coherent radiation propagation through the target interferometer for realizing port-to-port optical switches for each input port to each output port of the optical chip. In each visualization a special currents set  $\{x_1, x_2, x_3\}$  is applied to chips' tunable phase shifters in order to realize a corresponding switch. b) Histograms of the power distribution in the output ports of a device optimized for one-to-one switching to a specific output port.